Simulation of granular flow in a rotating frame of reference using the Discrete Element Method

Bastien Delacroix[a], Anya Bouarab[b], Louis Fradette[a], François Bertrand[a,*], Bruno Blais[a,*]

[a] *Research Unit for Industrial Flows Processes (URPEI), Department of Chemical Engineering, Polytechique Montréal, PO Box 6079, Stn Centre-Ville, Montréal, QC, Canada, H3C 3A7*

[b] *Center for Research in Computational Thermochemistry (CRCT), Department of Chemical Engineering, Polytechique Montréal, PO Box 6079, Stn Centre-Ville, Montréal, QC, Canada, H3C 3A7*

Abstract

Over the years, the Discrete Element Method (DEM) has attracted significant attention for its capacity to simulate granular flows because it captures physical phenomena that cannot be observed using continuum methods. However, the simulation of granular systems with DEM is computationally demanding, especially in the case of systems in rotation. One solution is to perform simulations in a non-inertial rotating frame of reference, which requires the addition of fictitious velocity-dependent forces such as the Coriolis force. We assess the numerical feasibility and accuracy of such DEM simulations. We show that the velocity Verlet scheme in its classical form no longer defines a symplectic map and is no longer of second order when there are velocity dependent forces. Nevertheless, our study of a dense particle flow within a rotating hourglass shows that the relevant properties of such flow are accurately reproduced in a non-inertial frame and that computational performance is improved.

Keywords: DEM, non-inertial frame, symplectic integrator, volume presearving scheme, Coriolis force, CFD-DEM

1. Introduction

Granular flows occur in many pharmaceutical, biomechanical and food processes, and the solids motion is critical to the final quality of the products.

*Corresponding authors

Email addresses: francois.bertrand@polymtl.ca (François Bertrand), bruno.blais@polymtl.ca (Bruno Blais)

The study of granular dynamics requires knowledge of a large number of particle properties, including density, size, size distribution, shape and rigidity. Moreover, experimental investigations can be difficult to set up and analyze [1]. Numerical modeling, which is complementary to experimental investigations, can facilitate the study of these systems.

While continuum methods have traditionally been preferred for studying granular flows, more recently there has been increased interest in Lagrangian approaches such as the Discrete Element Method (DEM). While DEM has proven accurate in a wide variety of applications, it is limited by its computational cost, which depends on the number of particles and the complexity of the geometry of the device. In pure granular flow studies, reasonable computational times can be achieved with up to 10^8 particles [2]. However, this is not the case for multiphase solid-fluid studies, for which the efficiency is even more limited, especially when the geometry is in motion (e.g., rotating) as is commonly encountered in industrial mixing, segregation and drying applications [3].

To avoid the problem of a rotating geometry (e.g. an impeller in a vessel), the simulation can be carried out in the rotating frame linked to the geometry that is in rotation. The physics behind studies of non-inertial frames has been known for a long time and is commonly used in computational fluid dynamics with numerical methods such as the single reference frame (SRF) and multiple reference frame (MRF) [4, 5]. However, this approach has not been extended to granular flows, and only two DEM studies have been performed in rotational frames. To the authors' knowledge, only Shirsath *et al* have dealt with this issue for the improvement of the computational performance of a rotating chute simulation, in particular when the granular flow is coupled with a fluid [6, 7]. Performing DEM in such a frame is challenging. Because of the non-inertial properties of these frames, inertial forces, i.e., centrifugal and Coriolis forces, have to be taken into account. The Coriolis force is peculiar because it depends on the velocity of the particles. In the present paper, we show that inertial forces pose a number of challenges for the numerical integration of the corresponding equation of motion.

For DEM simulations, symplectic integrators are often used, due to their energy conserving nature. The velocity Verlet integration scheme is one of the most commonly used schemes in the context of DEM and is currently implemented in many DEM open source codes such as YADE [8], MERCURY [9] and LAMMPS [10, 11], as well as LIGGGHTS [12], which was used in the present study.

It is important to note that velocity-dependent forces are not only relevant for non-inertial frames of reference. Increasing attention is now paid to the coupling between granular flows and magnetic fields [13, 14, 15], and the Lorentz force is a velocity-dependent force like the Coriolis force [16]. This underlines the fact that while velocity dependent forces are of great interest, few studies have focused specifically on their impact on numerical integration schemes [17, 18] and none have been done with specific applications to DEM.

The main goal of this work is to apply the Discrete Element Method in the context of a rotating geometry. In this paper we test the feasability of performing DEM simulations in a non-inertial frame and shed light on the impact of a velocity-dependent force such as the Coriolis force, on the accuracy and symplectic properties of a classical DEM integration scheme.

This paper is divided into three parts. The first (sections 2 and 3) provides a brief introduction to DEM and the physics of rotating frames. The second (sections 4, 5, 6 and 7) presents a theorical framework for the impacts of velocity-dependent forces on a symplectic integration scheme using simple problems. The third (sections 8 and 9) discusses the feasibility of using DEM in a non-inertial frame based on several schemes. It also discusses the impact of using rotating frames on computational performance.

2. Discrete Element Method

DEM is a Lagrangian approach for modeling granular flows where each particle is considered as a discrete entity. The method integrates Newton's second law of motion to calculate the velocity and position of each particle at every time step of the simulation.

The method specifically deals with collisions, which are detected by comparing the distance of two particles to the sum of their radii. If two particles overlap, a simple spring and dashpot model is used to compute a contact force that is decomposed into elastic and dissipative components. Each of these components is divided into a tangential and a normal term (Figure 1).

Based on Newton's second law of motion, the governing equations for the translational ($\boldsymbol{v}_i$) and rotational ($\boldsymbol{\omega}_{p,i}$) motions of particle i can be written as

[12, 19, 2]:

$$m_i \frac{d\boldsymbol{u}_i}{dt} = \sum_j \boldsymbol{f}_{c,ij} + \sum_k \boldsymbol{f}_{lr,ik} + \boldsymbol{f}_{g,i} \tag{1}$$

$$I_i \frac{d\boldsymbol{\omega}_{p,i}}{dt} = \sum_j \left(\boldsymbol{M}_{t,ij} + \boldsymbol{M}_{r,ij}\right) \tag{2}$$

where m_i is the mass of particle i, I_i the moment of inertia of particle i, $\boldsymbol{f}_{c,ij}$ the contact forces between particles i and j, $\boldsymbol{f}_{lr,ik}$ the non-contact (long-range) forces between particles i and k, $\boldsymbol{f}_{g,i}$ the gravitational force ($\boldsymbol{f}_{g,i} = m_i \boldsymbol{g}$), and $\boldsymbol{M}_{t,ij}$ and $\boldsymbol{M}_{r,ij}$ the tangential and rolling friction torques acting on particle i due to its contact with particle j. In the present work, non-contact forces, such as electrostatic or Van Der Waals forces were not taken into account due to the size and nature of the particles.

The contact forces between two particles were split into normal ($\boldsymbol{f}_{cn,ij}$) and tangential ($\boldsymbol{f}_{ct,ij}$) [20] components:

$$\boldsymbol{f}_{c,ij} = \boldsymbol{f}_{cn,ij} + \boldsymbol{f}_{ct,ij} = \quad k_{n,ij}\boldsymbol{\delta}_{n,ij} \quad \gamma_{n,ij}\dot{\boldsymbol{\delta}}_{n,ij} \quad k_{t,ij}\boldsymbol{\delta}_{t,ij} \quad \gamma_{t,ij}\dot{\boldsymbol{\delta}}_{t,ij} \tag{3}$$

where $k_{n,ij}$ and $k_{t,ij}$ are the normal and tangential stiffness coefficients, $\gamma_{n,ij}$ and $\gamma_{t,ij}$ the normal and tangential damping coefficients, $\boldsymbol{\delta}_{n,ij}$ and $\boldsymbol{\delta}_{t,ij}$ the normal and tangential overlaps, and $\dot{\boldsymbol{\delta}}_{n,ij}$ and $\dot{\boldsymbol{\delta}}_{t,ij}$ their derivatives with respect to time.

In the present work, we used a model proposed by Tsuji *et al.* [21] based on the Hertz theory [22] for the normal forces. We used the Mindlin model [23] for the tangential force. These models were combined to link the stiffness and damping coefficients to Young's modulus of the material (Y), the Poisson ratio (ν), and the coefficient of restitution (e_r), using the equations given in Table 1. The tangential overlap $\boldsymbol{\delta}_{t,ij}$ was truncated using Coulomb's law to ensure that $\boldsymbol{f}_{ct,ij} \rightarrow \quad \mu_{s,ij} \sqrt{\boldsymbol{f}_{cn,ij}} \frac{\boldsymbol{\delta}_{t,ij}}{|\boldsymbol{\delta}_{t,ij}|}$.

3. Non-inertial Frame of Reference

In a rotational frame of reference, Newton's equations of motion cannot be applied in their classical form since Coriolis ($\boldsymbol{F}_{coriolis}$) and centrifugal ($\boldsymbol{F}_{centrifugal}$) forces must be taken into account. The expression for these forces are:

$$\boldsymbol{F}_{coriolis} = \quad 2m\boldsymbol{\Omega} \pm \boldsymbol{v} \tag{4}$$

$$\boldsymbol{F}_{centrifugal} = \quad m\boldsymbol{\Omega} \pm (\boldsymbol{\Omega} \pm \boldsymbol{q}) \tag{5}$$

where $\boldsymbol{\Omega}$ is the rotation vector of the frame of reference, and $\boldsymbol{q}$ and $\boldsymbol{v}$ are the position (from the projection point on the axis of rotation: $\boldsymbol{q} \times \boldsymbol{\Omega} = 0$) and velocity vectors, respectively.
For larger particles, Coriolis torque must also be taken into account to ensure conservation of the angular momentum:

$$T_{coriolis} = \quad I(\boldsymbol{\Omega} \pm \boldsymbol{\omega}_p) \tag{6}$$

where $I = \frac{2}{5}mr^2$ is the inertial momentum of a solid sphere, r the radius, and ω_p the angular velocity. Due to the size of the particles in the present study ($d_p < 1cm$), we did not take the impact of this torque into account.

To evaluate the impact of the Coriolis and centrifugal forces compared to other inertial forces, we used the Rossby number, which is a dimensionless number typically used in geophysical studies. In granular dynamics, the Rossby number is defined as [24]:

$$R_0 = \frac{\boldsymbol{v}_{lag}}{2\Omega L sin(\phi)} \tag{7}$$

where $\boldsymbol{v}_{lag}$ is the characteristic particle flow velocity in the rotational frame of reference, L a characteristic length of the system, Ω the frame velocity, and ϕ a caracteristic angle of the position of the particle. In geophysics, for instance, this would be the latitude. When $R_o > 1$, the rotation has no significant impact on the system whereas $R_o << 1$ implies that the Coriolis force is considerable.

Lastly, simulations in a non-inertial frame of reference require a correct imposition of the initial velocity. As such, the velocity of the frame must be substracted from the initial Eulerian velocity to give the right initial condition in this non-inertial frame:

$$\boldsymbol{v}_{lag,t=0} = \boldsymbol{v}_{eul,t=0} \quad \boldsymbol{\Omega} \pm \boldsymbol{q} \tag{8}$$

4. Hamiltonian System and Symplectic Integration Scheme

4.1. Canonical formulation of the Hamiltonian mechanic

We begin by recalling the Newtonian description of a conservative system where all forces can be written as the negative gradient of a potential energy $V(q)$. Using the notation of [25] this can be written as:

$$m\frac{d^2\boldsymbol{q}}{dt^2} = \quad {}_q V(\boldsymbol{q}) \tag{9}$$

This second order equation can be transformed into a system of first order by considering the conjugate momenta defined as $p = \frac{\partial L}{\partial \dot{q}}$ with L the Lagrangian [26]. This redefinition of the problem based on a single total energy function, called the Hamiltonian (H), is given by:

$$\begin{cases} \frac{d\boldsymbol{q}}{dt} = & {}_{p}H(\boldsymbol{q},\boldsymbol{p}) \\ \frac{d\boldsymbol{p}}{dt} = & {}_{q}H(\boldsymbol{q},\boldsymbol{p}) \end{cases} \tag{10}$$

This system is the **canonical** formulation of Hamiltonian mechanics. It is important to note that the conjugate momenta is different from the momentum ($m\dot{\boldsymbol{q}}$). In some cases these quantities are not equal. Finally, we recall the general definition of an Hamiltonian system as:

$$m\frac{d\boldsymbol{z}}{dt} = J \quad {}_{z}H(\boldsymbol{z}) \tag{11}$$

where $\boldsymbol{z}$ represent the canonical variables $(\boldsymbol{q},\boldsymbol{p})$, J an arbitrary invertible constant skew-symmetric matrix and ${}_{z}$ the derivative with respect to the variable z. A **canonical** Hamiltonian system is defined as the particular case where the matrix J has following structure:

$$J = \begin{pmatrix} 0 & I_d \\ I_d & 0 \end{pmatrix} \tag{12}$$

4.2. Flow map and symplecticity

A physical problem is defined by an equation of motion $\dot{\boldsymbol{z}} = f(\boldsymbol{z})$ with an initial condition $\boldsymbol{z}^0$. We note the solution of such a problem $\boldsymbol{z}(t, z^0)$. The flow map $\Phi_{\tau,H}$ associated to a particular Hamiltonian H, is defined as the set of trajectories from $\boldsymbol{z}^0$ to the final point $\boldsymbol{z}(t = \tau, z^0)$. Thus:

$$\boldsymbol{z}(\tau, z^0) = \Phi_{\tau,H}(\boldsymbol{z}^0) \tag{13}$$

Symplecticity is a property associated to a flow map whose jacobian ($\Phi_z(\boldsymbol{z}) = \frac{\partial \Phi_{\tau,H}(\boldsymbol{z}^0)}{\partial \boldsymbol{z}}$) satisfies the following relation with the respect of specific structure matrix J [25]:

$$[\Phi_z(z)]^T J^{-1} [\Phi_z(z)] = J^{-1} \tag{14}$$

For example, the flow map of a canonical Hamiltonian system is symplectic [25]. The symplecticity is a very interesting property because it implies the existence of some conservation laws.

For example, if we consider the evolution of an element of volume in the phase space after an infinetisimal time δt, for a canonical Hamiltonian system we can write:

$$\boldsymbol{q}(t+\delta t) = \boldsymbol{q}(t) + \delta t \frac{\partial \boldsymbol{q}}{\partial t} + \wedge(\delta t^2) \tag{15}$$

$$\boldsymbol{p}(t+\delta t) = \boldsymbol{p}(t) + \delta t \frac{\partial \boldsymbol{p}}{\partial t} + \wedge(\delta t^2) \tag{16}$$

According to Hamilton's equations (10), it then follows that:

$$\boldsymbol{q}(t+\delta t) = \boldsymbol{q}(t) + \delta t \frac{\partial H}{\partial \boldsymbol{p}} + \wedge(\delta t^2) \tag{17}$$

$$\boldsymbol{p}(t+\delta t) = \boldsymbol{p}(t) \quad \delta t \frac{\partial H}{\partial \boldsymbol{q}} + \wedge(\delta t^2) \tag{18}$$

According to the change of variable theorem in an integral, the relation between the initial volume and the volume after an infinitesimal time step δt is given by the determinant of the Jacobian $\left(\frac{\partial(\boldsymbol{q}(t+\delta t),\boldsymbol{p}(t+\delta t)}{\partial(\boldsymbol{q}(t),\boldsymbol{p}(t))}\right)$ which corresponds to the determinant of the Jacobian of the flow map $\Phi_z(\boldsymbol{z})$:

$$det(\Phi_z(\boldsymbol{z})) = \left\| det \begin{pmatrix} 1+\delta t \frac{\partial^2 H}{\partial \boldsymbol{q}\partial \boldsymbol{p}} & & \delta t \frac{\partial^2 H}{\partial \boldsymbol{q}^2} \\ \delta t \frac{\partial^2 H}{\partial \boldsymbol{p}^2} & 1 & \delta t \frac{\partial^2 H}{\partial \boldsymbol{q}\partial \boldsymbol{p}} \end{pmatrix} \right\| = 1 + \wedge(\delta t)^2 \tag{19}$$

Lastly, with $\delta t \Leftrightarrow 0$ we can conclude that the flow map of canonical Hamiltonian system are volume preserving. In other words, the property of the Liouville-Poincaré invariant (Figure 2) [26] is respected if the determinant of the Jacobian matrix of a considered flow map is equal to 1.

Or, from the definition of the symplecticity (14) we can write:

$$det([\Phi_z(z)]^T J^{-1}[\Phi_z(z)]) = det(J^{-1}) \tag{20}$$

$$\in \ det([\Phi_z(z)]^T) det(J^{-1}) det([\Phi_z(z)]) = det(J^{-1}) \tag{21}$$

$$\in \quad det([\Phi_z(z)]) = 1 \tag{22}$$

Thus, a symplectic flow map conserves the volume in phase space. Moreover, a direct consequence of the symplectic property is the conservation of energy in time. A detailed demonstration of this property, via a backward error analysis is given in [25].

There is a more easily approachable definition of the symplectic property, which we will use in the rest of this study, via the differential of the wedge

product [27]:

$$d\boldsymbol{q}^{t+\delta t} \mid \; d\boldsymbol{p}^{t+\delta t} = d\boldsymbol{q}^{t} \mid \; d\boldsymbol{p}^{t} \tag{23}$$

$$\text{with} \quad \begin{pmatrix} \boldsymbol{q}^{t+\delta t} \\ \boldsymbol{p}^{t+\delta t} \end{pmatrix} = \Phi_{\delta t, H} \begin{pmatrix} \boldsymbol{q}^{t} \\ \boldsymbol{p}^{t} \end{pmatrix} \tag{24}$$

A demonstration of the equivalence between the definitions (14) and (23) is given in [25].

4.3. Symplectic integrator scheme

We have seen what symplecticity means for Hamiltonian systems, it is now interesting to understand how a numerical integrator could preserve this important property. In granular dynamics simulations, a class of integration schemes, the so-called symplectic integration schemes, are used to ensure the global conservation of energy in the absence of a dissipation mechanism (e.g. inelastic collisions). Numerous integration schemes are symplectic, including the Euler symplectic, Runge-Kutta symplectic and Verlet schemes [28]. The core idea behind these schemes is to update the position before computing the velocity within the same time step. One of the most common schemes used in granular dynamics, and particularly in the case of DEM, is the velocity Verlet scheme.

The velocity Verlet scheme [29] is based on updating the velocity at the half time step before updating the position. Then, calculating the acceleration using this position, the velocity is evaluated at the end of the time step. Its formulation, for the resolution of $\frac{\partial \boldsymbol{v}}{\partial t} = \boldsymbol{a}(\boldsymbol{q})$, with $\boldsymbol{a}$ the acceleration vector, is given by:

VELOCITY VERLET SCHEME

$$\begin{cases} \boldsymbol{v}^{n+1/2} = \boldsymbol{v}^{n} + \frac{\Delta t}{2}\boldsymbol{a}(\boldsymbol{q}^{n}) \\ \boldsymbol{q}^{n+1} = \boldsymbol{q}^{n} + \Delta t \boldsymbol{v}^{n+1/2} \\ \boldsymbol{v}^{n+1} = \boldsymbol{v}^{n+1/2} + \frac{\Delta t}{2}\boldsymbol{a}(\boldsymbol{q}^{n+1}) \end{cases} \tag{25}$$

This is a second order scheme for position and velocity [17].

Let's start by going back to the construction of such an integrator. This method is based on the fact that the Hamiltonian is separable, i.e. a Hamiltonian that can be written as a sum of a kinetic energy and a potential energy:

$$H(\boldsymbol{q},\boldsymbol{p}) = V(\boldsymbol{q}) + T(\boldsymbol{p}) \tag{26}$$

The method is based on a splitting into 3 parts:

$$H(\boldsymbol{q},\boldsymbol{p}) = H_1 + H_2 + H_3$$

$$\text{with} \quad H_1 = \frac{1}{2}V(\boldsymbol{q}) \quad H_2 = T(\boldsymbol{p}) \quad H_3 = \frac{1}{2}V(\boldsymbol{q}) \tag{27}$$

Thus the mapping $\Psi_{\Delta t,H}$ generated by the integrator during a time step Δt for a system, defined by its Hamiltonian H, is written as the composition of the 3 mappings of the splitting Hamiltonian:

$$\Psi_{\Delta t,H} = \Psi_{\frac{\Delta t}{2},V} \leq \Psi_{\Delta t,T} \leq \Psi_{\frac{\Delta t}{2},V} \tag{28}$$

According to the canonical Hamilton's equation (10), each mapping is associated with the following sub-systems:

$$\text{For} \quad H_1(\boldsymbol{q}) \quad \text{and} \quad H_3(\boldsymbol{q}) \quad \begin{cases} \frac{d\boldsymbol{q}}{dt} = 0 \\ \frac{d\boldsymbol{p}}{dt} = \quad {}_qV(\boldsymbol{q}) \end{cases} \tag{29}$$

$$\text{For} \quad H_2(\boldsymbol{p}) \quad \begin{cases} \frac{d\boldsymbol{q}}{dt} = \quad {}_pT(\boldsymbol{p}) \\ \frac{d\boldsymbol{p}}{dt} = 0 \end{cases} \tag{30}$$

From these equations we can derive the flow map for each term:

$$\Psi_{\frac{\Delta t}{2},V} = \begin{pmatrix} \boldsymbol{q} \\ \\ \boldsymbol{p} \quad \frac{\Delta t}{2} \quad {}_qV(\boldsymbol{q}) \end{pmatrix} \tag{31}$$

$$\Psi_{\Delta t,T} = \begin{pmatrix} \boldsymbol{q} + \Delta t \quad {}_pT(\boldsymbol{p}) \\ \\ \boldsymbol{p} \end{pmatrix} \tag{32}$$

We apply the composition (28) to a system $(\boldsymbol{q}^n, \boldsymbol{p}^n)^T$:

$$\Psi_{\frac{\Delta t}{2},V} = \begin{cases} \bar{\boldsymbol{q}} = \boldsymbol{q}^n \\ \\ \bar{\boldsymbol{p}} = \boldsymbol{p}^n \quad \frac{\Delta t}{2} \quad {}_qV(\boldsymbol{q}^n) \end{cases} \tag{33}$$

$$\Psi_{\Delta t,T} = \begin{cases} \bar{\bar{\boldsymbol{q}}} = \bar{\boldsymbol{q}} + \Delta t \quad {}_pT(\bar{\boldsymbol{p}}) \\ \\ \bar{\bar{\boldsymbol{p}}} = \bar{\boldsymbol{p}} \end{cases} \tag{34}$$

$$\Psi_{\frac{\Delta t}{2},V} = \begin{cases} \boldsymbol{q}^{n+1} = \bar{\bar{\boldsymbol{q}}} \\ \\ \boldsymbol{p}^{n+1} = \bar{\bar{\boldsymbol{p}}} \quad \frac{\Delta t}{2} \quad {}_qV(\bar{\bar{\boldsymbol{q}}}) \end{cases} \tag{35}$$

Finally if we identify $\bar{\boldsymbol{p}}$ as $\boldsymbol{p}^{n+1/2}$ and we concatenate each step we obtain:

$$\begin{cases} \boldsymbol{p}^{n+1/2} = \boldsymbol{p}^n \quad \frac{\Delta t}{2} \quad {}_qV(\boldsymbol{q}^n) \\ \\ \boldsymbol{q}^{n+1} = \boldsymbol{q}^n + \Delta t \quad {}_pT(\boldsymbol{p}^{n+1/2}) \\ \\ \boldsymbol{p}^{n+1} = \boldsymbol{p}^{n+1/2} \quad \frac{\Delta t}{2} \quad {}_qV(\boldsymbol{q}^{n+1}) \end{cases} \tag{36}$$

which correspond to the formulation of (25) in **canonical** coordinates with the conjugate momenta $\boldsymbol{p}$ equal to the momentum $m\dot{\boldsymbol{q}}$. To simplify the calculations we consider $m = 1$. The system (36) is equivalent to:

$$\begin{cases} \boldsymbol{q}^{n+1} = \boldsymbol{q}^n + \Delta t \boldsymbol{p}^n \quad \frac{\Delta t^2}{2} \quad {}_q V(\boldsymbol{q}^n) \\ \boldsymbol{p}^{n+1} = \boldsymbol{p}^n \quad \frac{\Delta t}{2} \quad {}_q V(\boldsymbol{q}^n) \quad \frac{\Delta t}{2} \quad {}_q V(\boldsymbol{q}^{n+1}) \end{cases} \tag{37}$$

Then, we differentiate these two equations:

$$\begin{cases} d\boldsymbol{q}^{n+1} = d\boldsymbol{q}^n + \Delta t d\boldsymbol{p}^n \quad \frac{\Delta t^2}{2} \quad {}_{qq} V(\boldsymbol{q}^n) d\boldsymbol{q}^n \\ d\boldsymbol{p}^{n+1} = d\boldsymbol{p}^{n+1/2} \quad \frac{\Delta t}{2} \quad {}_{qq} V(\boldsymbol{q}^n) d\boldsymbol{q}^n \quad \frac{\Delta t}{2} \quad {}_{qq} V(\boldsymbol{q}^{n+1}) d\boldsymbol{q}^{n+1} \end{cases} \tag{38}$$

with ${}_{qq}$ the Hessian matrix. Considering the wedge product between the two:

$$\begin{aligned} d\boldsymbol{q}^{n+1} \mid \; d\boldsymbol{p}^{n+1} = & d\boldsymbol{q}^{n+1} \mid \; d\boldsymbol{p}^n \\ & \frac{\Delta t}{2} d\boldsymbol{q}^{n+1} \mid \; (\quad {}_{qq} V(\boldsymbol{q}^n) d\boldsymbol{q}^n) \\ & \frac{\Delta t}{2} d\boldsymbol{q}^{n+1} \mid \; (\quad {}_{qq} V(\boldsymbol{q}^{n+1}) d\boldsymbol{q}^{n+1}) \end{aligned} \tag{39}$$

with

$$\begin{aligned} d\boldsymbol{q}^{n+1} \mid \; d\boldsymbol{p}^n = & d\boldsymbol{q}^n \mid \; d\boldsymbol{p}^n \\ & + \Delta t d\boldsymbol{p}^n \mid \; d\boldsymbol{p}^n \\ & \frac{\Delta t^2}{2} \quad {}_{qq} V(\boldsymbol{q}^n) d\boldsymbol{q}^n \mid \; d\boldsymbol{p}^n \end{aligned} \tag{40}$$

and

$$d\boldsymbol{q}^{n+1} \mid \left(\quad {}_{qq}V(\boldsymbol{q}^n) d\boldsymbol{q}^n \right) = d\boldsymbol{q}^n \mid \left(\quad {}_{qq}V(\boldsymbol{q}^n) d\boldsymbol{q}^n \right)$$

$$+ \Delta t d\boldsymbol{p}^n \mid \left(\quad {}_{qq}V(\boldsymbol{q}^n) d\boldsymbol{q}^n \right)$$

$$\frac{\Delta t^2}{2} \left(\quad {}_{qq}V(\boldsymbol{q}^n) d\boldsymbol{q}^n \right) \mid \left(\quad {}_{qq}V(\boldsymbol{q}^n) d\boldsymbol{q}^n \right) \qquad (41)$$

It is important to notice that the matrix ${}_{qq}V(\boldsymbol{q}^n)$ is a symmetric matrix, thus:

$$d\boldsymbol{q}^n \mid \left(\quad {}_{qq}V(\boldsymbol{q}^n) d\boldsymbol{q}^n \right) = 0 \qquad (42)$$

Finally, by replacing (40), (41) and (42) in (39) we obtain:

$$d\boldsymbol{q}^{n+1} \mid \; d\boldsymbol{p}^{n+1} = d\boldsymbol{q}^n \mid \; d\boldsymbol{p}^n \qquad (43)$$

This shows that, the velocity Verlet integration scheme defines a symplectic map or in other words the velocity Verlet scheme is symplectic.

We conclude the description of the velocity Verlet integrator by looking at the form of its flow map which could be described with the propagation matrix $R(\Delta t)$, for one time step:

$$\boldsymbol{z}^{n+1} = \Psi_{\Delta t, H}(\boldsymbol{z}^n) = R(\Delta t)\boldsymbol{z}^n \qquad (44)$$

We apply the velocity Verlet integration scheme for two close values of the position and the velocity $(\boldsymbol{q}_0, \boldsymbol{v}_0)$ and $(\boldsymbol{q}_0 + \delta\boldsymbol{q}_0, \boldsymbol{v}_0 + \delta\boldsymbol{v}_0)$, we obtain respectively

for the first step of (25):

$$\boldsymbol{v}_{1/2} = \boldsymbol{v}_0 + \frac{\Delta t}{2}\boldsymbol{a}(\boldsymbol{q}_0) \tag{45}$$

$$\boldsymbol{v}_{1/2} + \delta\boldsymbol{v}_{1/2} = \boldsymbol{v}_0 + \delta\boldsymbol{v}_0 + \frac{\Delta t}{2}\boldsymbol{a}(\boldsymbol{q}_0 + \delta\boldsymbol{q}_0) \tag{46}$$

with a limited development around $\delta\boldsymbol{q}_0$ and $\delta\boldsymbol{v}_0$:

$$\boldsymbol{a}(\boldsymbol{q}_0 + \delta\boldsymbol{q}_0) = \boldsymbol{a}(\boldsymbol{q}_0) + \delta\mathbf{q}_0\boldsymbol{a}'(\boldsymbol{q}_0) + \wedge(\delta\boldsymbol{q}_0)^2 \tag{47}$$

then, if we replace (47) in (46) and substract (45) from (46), we obtain:

$$\begin{pmatrix} \delta\boldsymbol{q}_0 \\ \\ \delta\boldsymbol{v}_{1/2} \end{pmatrix} = A_1 \begin{pmatrix} \delta\boldsymbol{q}_0 \\ \\ \delta\boldsymbol{v}_0 \end{pmatrix} \quad \text{with} \quad A_1 = \begin{pmatrix} 1 & 0 \\ \\ \frac{\Delta t}{2}\boldsymbol{a}'(\boldsymbol{q}_0) & 1 \end{pmatrix} \tag{48}$$

If we use the same method for the second and third steps:

$$\begin{pmatrix} \delta\boldsymbol{q}_1 \\ \\ \delta\boldsymbol{v}_{1/2} \end{pmatrix} = A_2 \begin{pmatrix} \delta\boldsymbol{q}_0 \\ \\ \delta\boldsymbol{v}_{1/2} \end{pmatrix} \quad \text{with} \quad A_2 = \begin{pmatrix} 1 & \Delta t \\ \\ 0 & 1 \end{pmatrix} \tag{49}$$

$$\begin{pmatrix} \delta\boldsymbol{q}_1 \\ \\ \delta\boldsymbol{v}_1 \end{pmatrix} = A_3 \begin{pmatrix} \delta\boldsymbol{q}_1 \\ \\ \delta\boldsymbol{v}_{1/2} \end{pmatrix} \quad \text{with} \quad A_3 = \begin{pmatrix} 1 & 0 \\ \\ \frac{\Delta t}{2}\boldsymbol{a}'(\boldsymbol{q}_1) & 1 \end{pmatrix} \tag{50}$$

Lastly, the velocity Verlet integration scheme can be written as the matrix

product of these three operations:

$$\begin{pmatrix} \delta \boldsymbol{q}_1 \\ \\ \delta \boldsymbol{v}_1 \end{pmatrix} = R(\Delta t) \begin{pmatrix} \delta \boldsymbol{q}_0 \\ \\ \delta \boldsymbol{v}_0 \end{pmatrix} \quad \text{with} \quad R(\Delta t) = A_3 A_2 A_1 \tag{51}$$

The determinant of this matrix:

$$det(R(\Delta t)) = det(A_3 A_2 A_1) = det(A_3) det(A_2) det(A_1) = 1 \tag{52}$$

This shows that the velocity Verlet integration scheme is also a volume preserving method as expected due to its symplectic nature.

In conclusion of this analysis, the classical velocity Verlet scheme implemented in LIGGGHTS is volume preserving, second order and symplectic. However, these properties are verified only for Hamiltonian systems with a **canonical** structure and with a **separable** Hamiltonian.

5. Application to the Harmonic Oscillator

To illustrate the properties of the velocity Verlet integrator, it is useful to begin with the simple example of the harmonic oscillator in one dimension (a spring of stiffness k) whose equation of motion is given by:

$$\frac{dv(q)}{dt} + w^2 q = 0 \qquad \text{with} \qquad w = \sqrt{\frac{k}{m}} \tag{53}$$

$$\text{i.e.} \qquad a(q) + w^2 q = 0 \tag{54}$$

where v and q reprensent the velocity and the position of the mass m at the end of the spring. Moreover the Hamiltonian description of such a system is given by:

$$H(p,q) = \frac{p^2}{2m} + k\frac{q^2}{2} \quad \text{with} \quad p = mv \tag{55}$$

With a matrix notation:

$$\begin{pmatrix} \dot{q} \\ \\ \dot{p} \end{pmatrix} = \begin{pmatrix} 0 & 1 \\ \\ 1 & 0 \end{pmatrix} \begin{pmatrix} kq \\ \\ \frac{p}{m} \end{pmatrix} \tag{56}$$

which corresponds to the description of a Hamiltonian system (11) with a **canonical** structure due to the form of the matrix J. Moreover, the Hamiltonian of this system is **separable**. Consequently, we conclude that the characteristic flow map of this system is symplectic and that the velocity Verlet integrator seems adapted to maintain symplecticity. This will be verified through an energetic study.

From equation (51) of Section 4.3, we write for the velocity Verlet integration scheme:

$$\begin{pmatrix} \delta \boldsymbol{q}_1 \\ \\ \delta \boldsymbol{v}_1 \end{pmatrix} = \begin{pmatrix} 1 & 0 \\ \\ \frac{\Delta t}{2}\omega^2 & 1 \end{pmatrix} \begin{pmatrix} 1 & \Delta t \\ \\ 0 & 1 \end{pmatrix} \begin{pmatrix} 1 & 0 \\ \\ \frac{\Delta t}{2}\omega^2 & 1 \end{pmatrix} \begin{pmatrix} \delta \boldsymbol{q}_0 \\ \\ \delta \boldsymbol{v}_0 \end{pmatrix} \tag{57}$$

$$R(\Delta t) = A_3 A_2 A_1 \quad \text{and} \quad det(R(\Delta t)) = 1 \tag{58}$$

Firstly, this shows that, for the case of a harmonic oscillator, the velocity Verlet scheme is volume preserving. From this equation, we can now look at the energy of the system. It can be shown that the eigenvalues of the matrix $R(\Delta t)$, λ_1 and λ_2 are given by:

$$\lambda_{1,2} = 1 \quad \frac{\Delta t^2 w^2}{2} \circ \; iw\Delta t\sqrt{1 \quad \frac{\Delta t^2 w^2}{4}} = r\exp(\circ\, i\theta) \tag{59}$$

$$\text{where} \qquad r = 1 \quad \text{and} \quad \theta = tan^{-1}\left(\frac{\Delta t w\sqrt{1 \quad \frac{\Delta t^2 w^2}{4}}}{1 \quad \frac{\Delta t^2 w^2}{2}}\right) \tag{60}$$

and the associated eigenvectors can be expressed by:

$$\boldsymbol{e}_1 = \begin{pmatrix} \frac{i}{w}\left(\sqrt{1 \quad \frac{\Delta t^2 w^2}{4}}\right)^{-1} \\ \\ 1 \end{pmatrix} \qquad \boldsymbol{e}_2 = \begin{pmatrix} \frac{i}{w}\left(\sqrt{1 \quad \frac{\Delta t^2 w^2}{4}}\right)^{-1} \\ \\ 1 \end{pmatrix} \tag{61}$$

From a simple recurrence, we can then write the relation between the n^{th} time step and the initial condition:

$$\begin{pmatrix} \boldsymbol{q}_n \\ \\ \boldsymbol{v}_n \end{pmatrix} = \begin{pmatrix} \boldsymbol{e}_1 & \boldsymbol{e}_2 \end{pmatrix} \begin{pmatrix} \lambda_1^n & 0 \\ \\ 0 & \lambda_2^n \end{pmatrix} \begin{pmatrix} \boldsymbol{e}_1 & \boldsymbol{e}_2 \end{pmatrix}^{-1} \begin{pmatrix} \boldsymbol{q}_0 \\ \\ \boldsymbol{v}_0 \end{pmatrix} \tag{62}$$

which is equivalent to:

$$\begin{pmatrix} \boldsymbol{q}_n \\ \\ \boldsymbol{v}_n \end{pmatrix} = \begin{pmatrix} cos(n\theta) & \frac{-1}{w\sqrt{1-\frac{\Delta t^2 w^2}{2}}} sin(n\theta) \\ \\ w\sqrt{1 \quad \frac{\Delta t^2 w^2}{2}} sin(n\theta) & cos(n\theta) \end{pmatrix} \begin{pmatrix} \boldsymbol{q}_0 \\ \\ \boldsymbol{v}_0 \end{pmatrix} \tag{63}$$

With $t = n\Delta t$, and in the particular case of $v_0 = 0$:

$$q(t) = q_0 cos(\frac{\theta t}{\Delta t}) \qquad v(t) = q_0\omega\frac{sin(\frac{\theta t}{\Delta t})}{\sqrt{1 \quad \frac{\Delta t^2 w^2}{4}}} \tag{64}$$

with this result, we can now calculate the energy of the system. It can be shown from the development of the argument of the eigenvalues at the 3^{rd} order that the energy at the 2^{nd} order is given by:

$$\theta = w\Delta t + \frac{w^3\Delta t^3}{24} + \wedge(\Delta t^4) \tag{65}$$

$$E = \frac{1}{2}mv^2 + \frac{1}{2}kq^2 \tag{66}$$

$$\text{i.e.} \quad E = \frac{1}{2}mq_0^2\omega^2\left(1 + \frac{\Delta t^2 w^2}{4}sin^2\left(\frac{\theta t}{\Delta t}\right)\right) + \wedge(\Delta t^3) \tag{67}$$

As expected, in the case of a harmonic oscillator with the velocity Verlet integration scheme, the energy is bounded ($\frac{2E}{mq_0^2w^2}$ / $[1, 1 + \frac{\Delta t^2 w^2}{4}]$) as shown by the periodic form of its expression (67).

We can make a similar development with another method such as the explicit Euler scheme, for example, and obtain:

$$J = \begin{pmatrix} 1 & h \\ \omega^2 h & 1 \end{pmatrix} \tag{68}$$

$$\lambda_{1,2} = 1 \circ \ iw\Delta t = r\exp(\circ\, i\theta) \tag{69}$$

$$\text{where} \qquad r = \sqrt{1 + \Delta t^2\omega^2} = 1 + \frac{\Delta t^2\omega^2}{2} + \wedge(\Delta t^3) \tag{70}$$

$$\text{and} \qquad \theta = tan^{-1}(\Delta t\omega) = \Delta t\omega + \wedge(\Delta t^3) \tag{71}$$

$$E = \frac{1}{2} m q_0^2 \omega^2 exp((\Delta t)t) + \wedge(\Delta t^2) \tag{72}$$

This shows that for a traditional non-symplectic explicit Euler scheme, the energy grows exponentially. Similarly, it could be shown that the second-order Runge-Kutta (RK2) and fourth-order Runge-Kutta (RK4) schemes are non-symplectic and do not conserve energy. We conclude that in presence of a separable canonical Hamiltonian system the energy is bounded if the velocity Verlet scheme is used. Generally, it is not the case for a non-symplectic integration scheme. This is illustrated in Figure 3, where different integration schemes, namely the symplectic velocity Verlet and non-symplectic explicit Euler, RK2 and RK4 schemes, were used for the harmonic oscillator system.

It is interesting to report the global order of these different integration schemes. These orders are highlighted by the error between the numerical and analytical solutions, $q(t) = q_0 cos(wt)$ after a finite time (Figure 4). The results obtained are those expected theoretically. In particular, the velocity Verlet scheme is second-order.

6. Velocity-dependent force

We have thus far shown that a symplectic integrator is generally required to stake out the energy of a system. However, if we consider the velocity Verlet scheme more carefully (25), we assumed that the acceleration, which is related to the forces felt by the particles, is only a function of the position. Therefore, it is unclear what occurs for the case of velocity-dependent forces. This question is essential for performing DEM simulations in a rotating frame because the Coriolis force is a velocity-dependent force.

In the case of a velocity-dependent force, the classical form of the explicit velocity Verlet scheme is following:

VELOCITY VERLET SCHEME

(With velocity-dependent force)

$$\begin{cases} \boldsymbol{v}^{n+1/2} = \boldsymbol{v}^n + \frac{\Delta t}{2}\boldsymbol{a}(\boldsymbol{q}^n, \boldsymbol{v}^{n-1/2}) \\ \boldsymbol{q}^{n+1} = \boldsymbol{q}^n + \Delta t \boldsymbol{v}^{n+1/2} \\ \text{Update acceleration} : \boldsymbol{a} = \boldsymbol{a}(\boldsymbol{q}^{n+1}, \boldsymbol{v}^{n+1/2}) \\ \boldsymbol{v}^{n+1} = \boldsymbol{v}^{n+1/2} + \frac{\Delta t}{2}\boldsymbol{a}(\boldsymbol{q}^{n+1}, \boldsymbol{v}^{n+1/2}) \end{cases} \tag{73}$$

We can immediately see that we evaluate the acceleration with a velocity and a position calculated at different instants.

To evaluate the consequences of this, we considered a damped oscillator. We

recall the projected equation of motion for a linear spring of stiffness k and a damper 2λ:

$$\frac{dv(q)}{dt} + 2\lambda v(q) + \omega^2 q = 0 \qquad \text{with} \qquad w = \sqrt{\frac{k}{m}} \tag{74}$$

First, we determined whether the velocity-dependent force has an impact on the global order of the scheme. In order to do so, we compared the numerical solution for the position with the analytical solution $x(t) = exp(\quad \lambda t)(q_0 cos(\omega_1 t) + \frac{\lambda q_0}{\omega} sin(\omega_1 t))$ with $w_1 = \nabla\overline{w^2 \quad \lambda^2}$ for the same integration schemes as before (Figure 5).

This example illustrates a first impact of a velocity-dependent force on the velocity Verlet scheme: it degrades from second to first order. We can see that this was not the case for the other integration schemes because the acceleration was not evaluated with a velocity and a position calculated at different instants. In the classical velocity Verlet scheme, the forces are calculated between the second and the third steps. However, if we examine (73), adding a new calculation of the forces before the beginning of the time step could be a solution to have the acceleration which depend on $\boldsymbol{q}_n, \boldsymbol{v}_n$ instead of $\boldsymbol{q}_n, \boldsymbol{v}_{n-1/2}$. The result is shown on Figure 5 with the "*Modified Velocity Verlet*" scheme, and we can see that there was an attenuation of the error, although it remains $\wedge\,(\Delta t)$. Since the

order of the scheme was unaffected by this modification, the classical velocity Verlet scheme was used subsequently in this work.

We recall that the main reason for using the velocity Verlet scheme in DEM simulation is that it is a symplectic integrator. The natural next step is to determine whether velocity-dependent forces have an impact on this important characteristic. This point will be investigated in the next section.

7. Velocity Verlet scheme with the Coriolis force

To assess the possibility of performing DEM simulations in a non-inertial frame of reference we need to understand the influence of the Coriolis force, which is a velocity dependent force, on symplectic integration schemes such as the velocity Verlet scheme. To evaluate this, we considered a particle in the Eulerian frame without any forces acting on it. In this frame, the particle was thus fixed. With a Newtonian formulation, the equation of motion of the same particle in the Lagrangian frame is given by:

$$m\frac{d^2\boldsymbol{q}_{lag}}{dt^2} = \quad 2m\boldsymbol{\Omega} \pm \frac{d\boldsymbol{q}_{lag}}{dt} \quad m\boldsymbol{\Omega} \pm (\boldsymbol{\Omega} \pm \boldsymbol{q}_{lag}) \tag{75}$$

where $\boldsymbol{q}_{lag}$ is the position vector in the Lagrangian frame, and $\boldsymbol{\Omega}$ the rotation vector equal to $(0 \quad 0 \quad w)$.

We start by changing the formalism by using the Hamiltonian description of the system in the non-inertial rotating frame of reference. The velocities in the two different frames are linked straightforwardly using:

$$\boldsymbol{v}_{eul} = \boldsymbol{v}_{lag} + \boldsymbol{\Omega} \pm \boldsymbol{q}_{lag} \tag{76}$$

where $\boldsymbol{v}_{lag}$ and $\boldsymbol{v}_{eul}$ are the velocity vectors in the Lagrangian and Eulerian frames.

Thus, the Lagrangian in the rotational frame is defined as:

$$L_{lag} = \frac{1}{2} m \boldsymbol{v}_{lag}^2 + m \boldsymbol{v}_{lag} (\boldsymbol{\Omega} \pm \boldsymbol{q}_{lag}) + \frac{1}{2} m (\boldsymbol{\Omega} \pm \boldsymbol{q}_{lag})^2 \tag{77}$$

with the Legendre transformation $H_{lag} = \boldsymbol{p}_{lag} \boldsymbol{v}_{lag} \quad L_{lag}$, where $\boldsymbol{p}_{lag}$ is the conjugate momenta in the rotational frame. We then deduced the Hamiltonian of this particle in the rotational frame of reference:

$$\boldsymbol{p}_{lag} = \frac{\partial L_{lag}}{\partial \boldsymbol{v}_{\boldsymbol{lag}}} = m \boldsymbol{v}_{lag} + m (\boldsymbol{\Omega} \pm \boldsymbol{q}_{lag}) \tag{78}$$

$$H_{lag} = \frac{(\boldsymbol{p}_{lag} \quad m(\boldsymbol{\Omega} \pm \boldsymbol{q}_{lag}))^2}{2m} \quad \frac{m}{2} (\boldsymbol{\Omega} \pm \boldsymbol{q}_{lag})^2 \tag{79}$$

The first term of this Hamiltonian represents the kinetic energy of the system

and the second term represents the centrifugal potential. Then, we can calculate:

$$\begin{cases} {}_{q_{lag}}H = \boldsymbol{\Omega} \pm \boldsymbol{p}_{lag} \\ {}_{p_{lag}}H = \frac{\boldsymbol{p}_{lag}}{m} \quad (\boldsymbol{\Omega} \pm \boldsymbol{q}_{lag}) \end{cases} \tag{80}$$

Finally, we deduce the associated canonical equations of motion which are equivalent to (75):

$$\begin{pmatrix} \dot{\boldsymbol{q}}_{lag} \\ \\ \dot{\boldsymbol{p}}_{lag} \end{pmatrix} = \begin{pmatrix} 0 & Id \\ \\ Id & 0 \end{pmatrix} \begin{pmatrix} \boldsymbol{\Omega} \pm \boldsymbol{p}_{lag} \\ \\ \frac{p_{lag}}{m} \quad (\boldsymbol{\Omega} \pm \boldsymbol{q}_{lag}) \end{pmatrix} \tag{81}$$

This equation gives the description of a canonical Hamiltonian system. However, if we look at the structure of the Hamiltonian (79) we can see that this one is not separable, which goes against the construction of the classical velocity Verlet scheme (section 4.3). To evaluate the impact of the non-separable Hamiltonian on this integration scheme we make a simple simulation of the particle in the rotating frame of reference. Since the particle is static in the Eulerian frame ($\boldsymbol{v}_{eul} = 0$), the expected trajectory in the Lagragian frame is a circle with a radius that depends on the initial position and the expected total energy is 0 ($E_{tot}(t) = H_{lag}(t) = 0$). Figure 6 shows a time step-dependent deviation of the particle from the theorical circular trajectory and an exponential growth of the total energy in time.

Thus, the consequence of a non-separable Hamiltonian is a non-conservation

of the energy when the classical explicit form of the velocity Verlet scheme is used. This is perfectly consistent with the demonstration of Sanz and Serna [30] which proved that symplectic methods are always implicit for generic Hamiltonians (i.e. not necessarily separable). In our case this implies that we reformulate the Verlet scheme following methods such as the partitioned Runge-Kutta method combined with the Lobatto IIIA and IIIB methods [31]. In this case the first step of the scheme would become implicit: $\boldsymbol{v}^{n+1/2} = \boldsymbol{v}^n + \frac{\Delta t}{2}\boldsymbol{a}(\boldsymbol{q}^n, \boldsymbol{v}^{n+1/2})$.

However, another approach consists in using splitting methods by reformulating the problem with a separable Hamiltonian. Thus, by considering $\boldsymbol{p}_{lag} = m\boldsymbol{v}_{lag}$, the first-order system is obtained from the equation of motion (75).

$$\begin{cases} \frac{d\boldsymbol{q}_{lag}}{dt} = \frac{\boldsymbol{p}_{lag}}{m} \\ \frac{d\boldsymbol{p}_{lag}}{dt} = \quad 2\boldsymbol{\Omega} \pm \boldsymbol{p}_{lag} \quad m\boldsymbol{\Omega} \pm (\boldsymbol{\Omega} \pm \boldsymbol{q}_{lag}) \end{cases} \tag{82}$$

It is easy to show that this system is not canonical. Indeed, let us suppose the contrary by considering that this Hamiltonian system has a canonical structure. For such an H it would have to hold that:

$$\begin{cases} {}_{q_{lag}}H = \quad \dot{\boldsymbol{p}}_{lag} = 2\boldsymbol{\Omega} \pm \boldsymbol{p}_{lag} + m\boldsymbol{\Omega} \pm (\boldsymbol{\Omega} \pm \boldsymbol{q}_{lag}) \\ {}_{p_{lag}}H = \dot{\boldsymbol{q}}_{lag} = \frac{\boldsymbol{p}_{lag}}{m} \end{cases} \tag{83}$$

We can show that these equations contradict Schwarz's Theorem, which states

that the second derivatives (i.e. $\frac{\partial^2 H}{\partial \boldsymbol{p} \partial \boldsymbol{q}} = \frac{\partial^2 H}{\partial \boldsymbol{q} \partial \boldsymbol{p}}$) are symmetric. Thus, we conclude that this system does not have a canonical structure.

However, it is a Hamiltonian system. Indeed system (82) is equivalent to:

$$\begin{pmatrix} \dot{\boldsymbol{q}}_{lag} \\ \dot{\boldsymbol{p}}_{lag} \end{pmatrix} = \begin{pmatrix} 0 & Id \\ Id & 2m\boldsymbol{\Omega}\pm \end{pmatrix} \begin{pmatrix} {}_{q_{lag}} H \\ {}_{p_{lag}} H \end{pmatrix} \tag{84}$$

with $H = \frac{|\boldsymbol{p}_{lag}|^2}{2m}$ $\quad \frac{m}{2} \sqrt{\boldsymbol{\Omega} \pm \boldsymbol{q}_{lag}}^2$

With this description we can build a splitting method inspired by the construction of the velocity Verlet method seen in section 4.3. We will use the method of Scovel [25]. We recall here the guidelines of this method. Firstly, we use the same splitting as for the classic velocity Verlet scheme:

$$\Psi_{\Delta t,H} = \Psi_{\frac{\Delta t}{2},V} \leq \Psi_{\Delta t,T} \leq \Psi_{\frac{\Delta t}{2},V} \tag{85}$$

with $V(\boldsymbol{q}_{lag}) = \quad \frac{m}{2} \sqrt{\boldsymbol{\Omega} \pm \boldsymbol{q}_{lag}}^2$ and $T(\boldsymbol{p}_{lag}) = \frac{|\boldsymbol{p}_{lag}|^2}{2m}$.

According to Equation (84), each mapping is associated with the following sub-systems:

$$\text{For} \quad \Psi_{\frac{\Delta t}{2},V} \quad \begin{cases} \frac{d\boldsymbol{q}_{lag}}{dt} = 0 \\ \frac{d\boldsymbol{p}_{lag}}{dt} = \quad {}_q V(\boldsymbol{q}) \end{cases} \tag{86}$$

$$\text{For} \quad \Psi_{\Delta t,T} \quad \begin{cases} \frac{d\boldsymbol{q}_{lag}}{dt} = \frac{\boldsymbol{p}_{lag}}{m} \\ \frac{d\boldsymbol{p}_{lag}}{dt} = \quad 2m\boldsymbol{\Omega} \pm \frac{\boldsymbol{p}_{lag}}{m} \end{cases} \tag{87}$$

The integration of the system (86) is exactly like in Section 4.3 (Eq.31). However, for the system (87) we solve:

$$\frac{d\boldsymbol{p}_{lag}}{dt} = \hat{\Omega}\boldsymbol{p}_{lag} \quad \text{with} \quad \hat{\Omega} = \begin{pmatrix} 0 & 2w & 0 \\ 2w & 0 & 0 \\ 0 & 0 & 0 \end{pmatrix} \tag{88}$$

The solution of this differential equation is: $\boldsymbol{p}_{lag}(t) = exp(\hat{\Omega}t)\boldsymbol{p}_{lag}(0)$. Thus, we can integrate the position:

$$\boldsymbol{q}_{lag}(t) = \boldsymbol{q}_{lag}(0) + \frac{1}{m}\int_0^t exp(\hat{\Omega}s)\boldsymbol{p}_{lag}(0)ds \tag{89}$$

Finally, if we concatenate each step with the respect of the equation (85) we obtain the explicit Scovel's scheme (90) which is an adaptation of the velocity Verlet's scheme.

SCOVEL SCHEME

$$\begin{cases} \boldsymbol{p}^{n+1/2} = \boldsymbol{p}^n \quad \frac{\Delta t}{2} \quad {}_qV(\boldsymbol{q}) \\ \boldsymbol{q}^{n+1} = \boldsymbol{q}^n + \frac{1}{m}\int_0^{\Delta t} exp(\hat{\Omega}s)\boldsymbol{p}^{n+1/2}ds \\ \boldsymbol{p}^{n+1} = exp(\hat{\Omega}\Delta t)\boldsymbol{p}^{n+1/2} \quad \frac{\Delta t}{2} \quad {}_qV(\boldsymbol{q}^{n+1}) \end{cases} \tag{90}$$

To calculate the exponential of the matrix we used the Rodrigues formula [25]:

$$exp(\hat{\Omega}t) = Id + \frac{sin(wt)}{w}\hat{\Omega} + 2\left(\frac{sin(wt/2)}{w}\right)^2\hat{\Omega}^2 \tag{91}$$

We performed the same simulations as before with this new scheme. The result of the simulations made with the Scovel scheme are presented in Figure 7.

As expected we observe that the energy is conserved and oscillates between the theoretical value $E_{tot} = 0$ and the value of the global numerical error which is time step-dependent. We note that the error committed on this energy is much lower than in the case of the velocity Verlet scheme.

Then we evaluate the numerical error on the position. This is illustrated in Figure 8 and compared with other integration schemes. This Figure leads to the same conclusions as Section 6: a velocity-dependent force leads to a degradation of the global order of convergence of the classical velocity Verlet scheme. However, Scovel's scheme preserves second order.

Finally, it is also interesting to note that the addition of the Coriolis force leads to the new velocity Verlet mapping:

$$A_1 = \begin{pmatrix} 1 & 0 \\ \frac{\Delta t}{2} \; {}_{q_0}\boldsymbol{a}(\boldsymbol{q}_0, \boldsymbol{v}_0) & 1 + \frac{\Delta t}{2} \; {}_{\boldsymbol{v}_0}\boldsymbol{a}(\boldsymbol{q}_0, \boldsymbol{v}_0) \end{pmatrix} \tag{92}$$

$$A_2 = \begin{pmatrix} 1 & \Delta t \\ 0 & 1 \end{pmatrix} \tag{93}$$

$$A_3 = \begin{pmatrix} 1 & 0 \\ \frac{\Delta t}{2} \quad {}_{\boldsymbol{q}_1}\boldsymbol{a}(\boldsymbol{q}_1, \boldsymbol{v}_{1/2}) & 1 + \frac{\Delta t}{2} \quad {}_{\boldsymbol{v}_{1/2}}\boldsymbol{a}(\boldsymbol{q}_1, \boldsymbol{v}_{1/2}) \end{pmatrix} \tag{94}$$

where $R(\Delta t) = A_3 A_2 A_1$ with $det(R(\Delta t)) \Cancel{=} 1$. Thus, another consequence is the loss of the volume preservation property of the classical velocity Verlet scheme with the addition of a velocity dependent force.

To sumarize, the explicit velocity Verlet scheme in its classical form is not the most appropriate integration scheme for systems with velocity-dependent forces and no source of dissipation. Indeed, in this case this scheme is not volume preserving, it is not second order for position and velocity and it does not conserve the symplecticity property of the system flow map. For such systems it is preferable to use symplectic implicit schemes or schemes constructed using a splitting method such as the Scovel scheme (Eq.90).

8. Verification with Damping Forces

The various impacts described in the previous section raise the question as to whether it is still justified to use the velocity Verlet scheme in the case of velocity-dependent forces. Indeed, the impacts of the loss of energy conservation were marked for simulations in a rotating frame of reference without dissipative forces. In real cases, dissipative forces tend to stabilize DEM simulations.

Therefore, we evaluated the possibility of performing DEM simulations in a rotating frame of reference for practical purposes using the classical velocity Verlet scheme (25) implemented in LIGGGHTS. Consequently, the simulations described in this section and the following ones were performed directly with the LIGGGHTS open source DEM software.

8.1. Verification with one particle

For the first test case, we put one particle on a disk and compared the trajectory of the particle in the two different frames of reference: the Eulerian frame where the disk was in rotation and the Lagrangian frame where the disk was fixed. In the Lagrangian frame, we added Coriolis and centrifugal forces (4) and (5) to the DEM equations.

We began with an analytical study of the trajectory of the particle in the Lagrangian frame. Indeed, contrary to the previous section, $\boldsymbol{v}_{eul} \neq 0$, and the expected trajectory is no longer a circle.

Based on the canonical formulation for a particle in the rotational frame previously obtained, the equations of the movement of a particle in this frame are:

$$\begin{cases} \dot{\boldsymbol{q}}_{lag} = \frac{\boldsymbol{p}_{\boldsymbol{lag}}}{m} \quad \boldsymbol{\Omega} \pm \boldsymbol{q}_{lag} \\ \dot{\boldsymbol{p}}_{lag} = \quad \boldsymbol{\Omega} \pm \boldsymbol{p}_{lag} \end{cases} \tag{95}$$

Using a matrix notation for the position equation and using $\boldsymbol{\Omega} = (0 \quad 0 \quad w)$, we obtain:

$$\dot{\boldsymbol{q}}_{lag} = \quad A\boldsymbol{q}_{lag} + \frac{\boldsymbol{p}_{lag}}{m} \qquad \text{with} \qquad A = \begin{pmatrix} 0 & w & 0 \\ w & 0 & 0 \\ 0 & 0 & 0 \end{pmatrix} \tag{96}$$

where A is a matrix that represents a rotation in a plane perpendicular to the z axis i.e., in the $x \quad y$ plane.

Due to the form of (96), the use of homogeneous coordinates rather than Cartesian coordinates was justified. We thus add a fictitious third coordinate to our system in two dimensions. It then follows that:

$$\begin{pmatrix} \dot{q}_{lag,x} \\ \dot{q}_{lag,y} \\ 1 \end{pmatrix} = \frac{1}{m} \begin{pmatrix} 1 & 0 & p_{lag,x} \\ 0 & 1 & p_{lag,y} \\ 0 & 0 & 1 \end{pmatrix} \begin{pmatrix} 0 & w & 0 \\ w & 0 & 0 \\ 0 & 0 & 1 \end{pmatrix} \begin{pmatrix} q_{lag,x} \\ q_{lag,y} \\ 1 \end{pmatrix} \tag{97}$$

or, more simply:

$$\begin{pmatrix} \dot{q}_{lag,x} \\ \dot{q}_{lag,y} \\ 1 \end{pmatrix} = \frac{1}{m} \begin{pmatrix} 0 & w & p_{lag,x} \\ w & 0 & p_{lag,y} \\ 0 & 0 & 1 \end{pmatrix} \begin{pmatrix} q_{lag,x} \\ q_{lag,y} \\ 1 \end{pmatrix} \tag{98}$$

With this equation of motion, we deduce that the trajectory in the rotational frame of this particle on a disk is a combination of a translation and a rotation in the opposite direction of the frame. We thus expected to obtain a spiral in this frame. The shape of this spiral will depend on the rotational speed and the friction between the disk and the particle.

As expected, we obtain the right trajectory with the numerical simulation using the LIGGGHTS software (Figure 9 (b)). Figure 9 also shows the trajectories of the particle with simulations in the two different frames. Then to compare these results we rotated the coordinates and we observed an exact agreement between the two simulations. Based on this conclusive result, we then performed a more complex experiment with more particles.

8.2. Verification with N particles

We simulated the motion of many particles in a rotating hourglass in the two different frames of reference: in the Eulerian frame, in which case the hourglass

rotated and in the Lagrangian frame, in which case the hourglass was fixed and Coriolis and centrifugal forces were added for each particle. All the physical parameters used for these simulations are presented in Table 2.

The main difference between this case and the previous one, with only one particle, is that the rotation is perpendicular to gravity. We thus considered the rotation of this force accordingly in the Lagrangian frame of reference. Figure 10 shows an illustration of the motion of the particle in both frames of reference at different instants. As can be seen, there is an exact agreement as regards to the motion of these particles in the two frames.

Next, we compared the evolution in time of the mass of particles in the bottom part of the hourglass for two different frame velocities. These two velocities were chosen based on the difference in the Rossby number (see (7)), which implied that the Coriolis and centrifugal forces have different impacts. Indeed, at 30 rpm, the particles were in motion during the rotation of the hourglass ($R_o = 0.5$) unlike at 120 rpm ($R_o = 0$), where particles remained stuck to the wall of the hourglass due to the greater impact of the non-inertial forces. Thus, for the larger frame velocity, there was no-slip between the wall and the particles during the rotation of the hourglass. This is shown in Figures 10 and 11, which illustrate the motion of the particles and where we can see that we still

have a similar behaviour of the particles at 120 rpm in the two different frames. Moreover, Figures 12 and 13 show that the evolution of the mass in the bottom part of the hourglass is exactly the same for simulations performed in Eulerian and Lagrangian frame of reference.

9. Computational Performance Study

Finally, for the sake of completeness, we investigated the impact on computational performance of conducting simulations in a rotating frame or reference. We performed the hourglass simulation in the two different frames, with different numbers of CPU. The cores were distributed symmetrically in the x-y plane, and the z axis was not partitioned, as illustrated in Figure 14. The difference in computational time between the simulations in the two frames is illustrated in Figure 15.

With this study, we conclude that increasing the number of CPU results in a 25% improvement in computational performance when conducting parallel (4 or 16 CPU) simulations in the rotating frame compared to traditional DEM simulations.

10. Conclusion

The main objective of this study was to model granular flows in rotating frame of reference using the discrete element method. Through our various investigations we showed that a velocity-dependent force such as the Coriolis force leads to non-canonical Hamiltonian systems or non-separable Hamiltonians. We explained why this is problematic if the classical velocity Verlet integrator, as it is implemented in LIGGGHTS, is used. We shed light on the fact that for these systems this integration scheme is first order, it does not define a symplectic map and it is not volume preserving. In the case of DEM, it is commonly accepted that a physical model requires global energy conservation [32], which is generally why all DEM open source software use the symplectic velocity Verlet scheme. This work revealed that, in the case of non-dissipative velocity-dependent forces such as Coriolis and Lorentz forces, the use of the classical velocity Verlet scheme is debatable and that more accurate results can be obtained with more appropriate scheme susch as the Scovel method.

In a non-inertial frame, with the classical velocity Verlet scheme implemented in LIGGGHTS, our results showed that the loss of the symplectic and volume preserving characteristic of the velocity Verlet scheme for DEM in a rotating

frame is not problematic because the dissipative forces stabilize the entire system. We obtained similar results in the Eulerian and Lagrangian frames for the test cases investigated, with better computational performance in the Lagrangian frame.

In summary, we showed in this work that it is possible to perform DEM simulations in a non-inertial frame although the use of the classic velocity Verlet scheme may be inappropriate if the Coriolis force or other non-dissipative velocity-dependent forces are dominant. In this case different solutions are possible. The first is to use implicit symplectic schemes such as the implicit partitioned Runge-Kutta scheme combined with Lobatto IIIA/B methods. Another solution is to use splitting methods. For example, we showed that the explicit Scovel scheme allows to recover a second order convergence and a symplectic flow map for simulations in non-inertial frame with the Coriolis force.

11. Acknowledgements

The financial support from the Natural Sciences and Engineering Research Council of Canada (NSERC) is gratefully acknowledged. Computations were made on supercomputers Cedar and Graham managed by Calcul Québec. In particular, the authors would like to acknowledge the efficient support received

from Calcul Québec systems analysts. Finally, we would like to thank Dr. Jason Franck from the University of Utrecht for his comments which greatly improved the depth and rigor of the present work.

References

[1] E. Alizadeh, F. Bertrand, J. Chaouki, Comparison of DEM results and Lagrangian experimental data for the flow and mixing of granules in a rotating drum, AIChE Journal 60 (1) (2014) 60–75.

[2] B. Blais, D. Vidal, F. Bertrand, G. S. Patience, J. Chaouki, Experimental Methods in Chemical Engineering: Discrete Element Method—DEM, The Canadian Journal of Chemical Engineering 97 (7) (2019) 1964–1973. doi:10.1002/cjce.23501.

[3] B. Blais, M. Lassaigne, C. Goniva, L. Fradette, F. Bertrand, Development of an unresolved CFD–DEM model for the flow of viscous suspensions and its application to solid–liquid mixing, Journal of Computational Physics 318 (2016) 201–221. doi:10.1016/j.jcp.2016.05.008.

[4] C. Hirsch, Numerical Computation of Internal and External Flows: The Fundamentals of Computational Fluid Dynamics, Elsevier, 2007.

[5] B. Blais, M. Lassaigne, C. Goniva, L. Fradette, F. Bertrand, A semi-implicit immersed boundary method and its application to viscous mixing, Computers & Chemical Engineering 85 (2016) 136–146. doi:10.1016/j.compchemeng.2015.10.019.

[6] S. S. Shirsath, J. T. Padding, J. A. M. H. Kuipers, H. J. H. Clercx, Simulation study of the effect of wall roughness on the dynamics of granular flows in rotating semicylindrical chutes, AIChE Journal 61 (7) (2015) 2117–2135. doi:10.1002/aic.14828.

[7] S. S. Shirsath, J. T. Padding, J. a. M. Kuipers, T. W. J. Peeters, H. J. H. Clercx, Numerical Investigation of Monodisperse Granular Flow Through an Inclined Rotating Chute, AIChE Journal 60 (10) (2014) 3424–3441. doi:10.1002/aic.14535.

[8] J. Kozicki, F. V. Donzé, YADE-OPEN DEM: An open-source software using a discrete element method to simulate granular material, Engineering Computations (Oct. 2009). doi:10.1108/02644400910985170.

[9] A. R. Thornton, D. Krijgsman, R. H. A. Fransen, S. G. Briones, D. R. Tunuguntla, A. te Voortwis, S. Luding, O. Bokhove, T. Weinhart, Mercury-

DPM: Fast particle simulations in complex geometries, EnginSoft newsletter simulation based engineering & sciences 10 (1) (2013) 48–53.

[10] S. Plimpton, Fast parallel algorithms for short-range molecular dynamics, Tech. rep., Sandia National Labs., Albuquerque, NM (United States) (1993).

[11] J. W. Landry, G. S. Grest, L. E. Silbert, S. J. Plimpton, Confined granular packings: Structure, stress, and forces, Physical review E 67 (4) (2003) 041303.

[12] LIGGGHTS. (2011). LAMMPS improved for general granular and granular heat transfer simulations. Retrieved from http://www.liggghts.com.

[13] X. Deng, J. V. Scicolone, R. N. Davé, Discrete element method simulation of cohesive particles mixing under magnetically assisted impaction, Powder Technology 243 (2013) 96–109. doi:https://doi.org/10.1016/j.powtec.2013.03.043.

[14] R. Soda, K. Takagi, K. Ozaki, Numerical simulation of magnetic-aligned compaction with pulsed high magnetic field, Scripta Materialia 120 (2016) 41–44. doi:https://doi.org/10.1016/j.scriptamat.2016.04.028.

[15] J. Lindner, K. Menzel, H. Nirschl, Simulation of magnetic suspensions for HGMS using CFD, FEM and DEM modeling, Computers & Chemical Engineering 54 (2013) 111–121.

[16] W. Benenson, J. W. Harris, H. Stöcker, H. Lutz, Handbook of Physics, Springer Science & Business Media, 2006.

[17] Q. Spreiter, M. Walter, Classical Molecular Dynamics Simulation with the Velocity Verlet Algorithm at Strong External Magnetic Fields, Journal of Computational Physics 152 (1) (1999) 102–119. doi:10.1006/jcph.1999.6237.

[18] C. Hellström, S. Mikkola, Explicit algorithmic regularization in the few-body problem for velocity-dependent perturbations, Celestial Mechanics and Dynamical Astronomy 106 (2) (2010) 143–156. doi:10.1007/s10569-009-9248-8.

[19] H. P. Zhu, Z. Y. Zhou, R. Y. Yang, A. B. Yu, Discrete particle simulation of particulate systems: A review of major applications and findings, Chemical Engineering Science 63 (23) (2008) 5728–5770. doi:10.1016/j.ces.2008.08.006.

[20] H. P. Zhu, Z. Y. Zhou, R. Y. Yang, A. B. Yu, Discrete particle simulation

of particulate systems: Theoretical developments, Chemical Engineering Science 62 (13) (2007) 3378–3396. doi:10.1016/j.ces.2006.12.089.

[21] Y. Tsuji, T. Tanaka, T. Ishida, Lagrangian numerical simulation of plug flow of cohesionless particles in a horizontal pipe, Powder Technology 71 (3) (1992) 239–250. doi:10.1016/0032-5910(92)88030-L.

[22] K. L. JOHNSON, Normal contact of elastic solids : Hertz theory, Contact Mechanics (1989) 84–106.

[23] R. D. MINDLIN, Elastic Spheres in Contact Under Varying Oblique Forces, J. Applied Mech. 20 (1953) 327–344.

[24] S. Shirsath, J. Padding, N. Deen, H. Clercx, J. Kuipers, Experimental study of monodisperse granular flow through an inclined rotating chute, Powder Technology 246 (2013) 235–246. doi:10.1016/j.powtec.2013.05.022.

[25] B. Leimkuhler, S. Reich, Simulating Hamiltonian Dynamics, Vol. 14, Cambridge university press, 2004.

[26] H. Goldstein, Classical Mechanics, Pearson Education, 2002.

[27] W. Rudin, Principles of Mathematical Analysis, Vol. 3, McGraw-hill New York, 1964.

[28] K. Feng, M. Qin, Symplectic Geometric Algorithms for Hamiltonian Systems, Springer, 2010.

[29] L. Verlet, Computer "Experiments" on Classical Fluids. I. Thermodynamical Properties of Lennard-Jones Molecules, Phys. Rev. 159 (1) (1967) 98–103. doi:10.1103/PhysRev.159.98.

[30] J. M. Sanz-Serna, Symplectic integrators for Hamiltonian problems: An overview, Acta numerica 1 (1992) 243–286.

[31] E. Hairer, C. Lubich, G. Wanner, Geometric Numerical Integration: Structure-Preserving Algorithms for Ordinary Differential Equations, Vol. 31, Springer Science & Business Media, 2006.

[32] H. R. Norouzi, R. Zarghami, R. Sotudeh-Gharebagh, N. Mostoufi, Coupled CFD-DEM Modeling: Formulation, Implementation and Application to Multiphase Flows, John Wiley & Sons, 2016.

[33] S. M. Derakhshani, D. L. Schott, G. Lodewijks, Micro–macro properties of quartz sand: Experimental investigation and DEM simulation, Powder Technology 269 (2015) 127–138. doi:10.1016/j.powtec.2014.08.072.

12. Figures

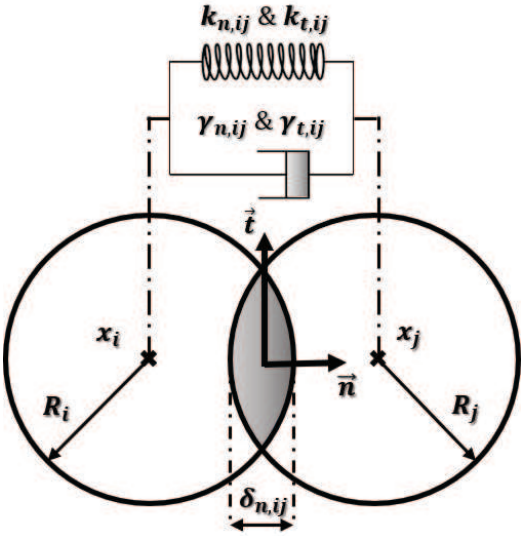

Figure 1: Illustration of the principle of the Discrete Element Method

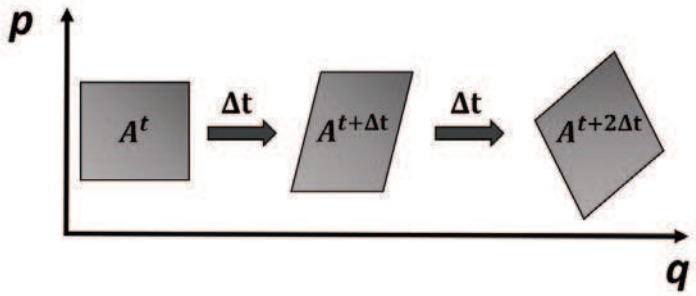

Figure 2: Illustration of the Liouville-Poincaré invariant: $A^t = A^{t+\Delta t} = A^{t+2\Delta t}$.

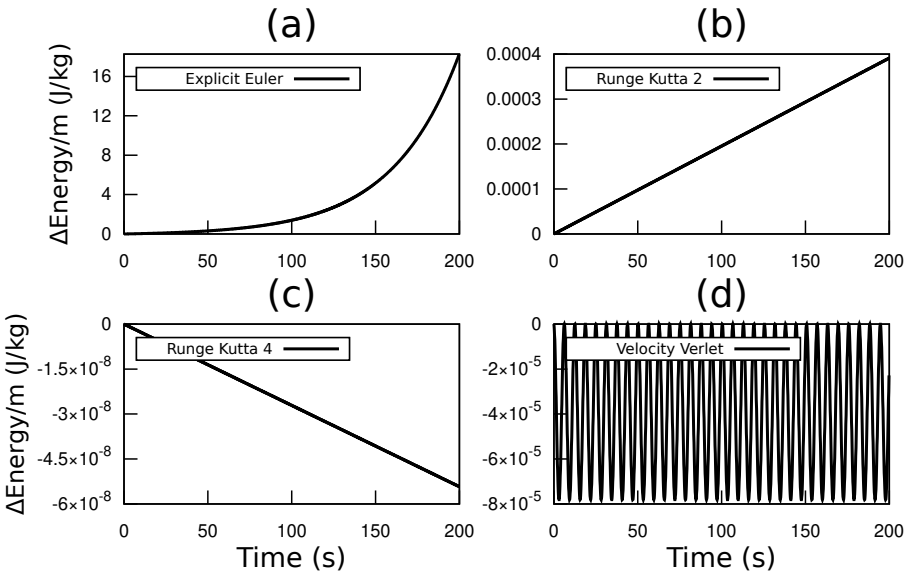

Figure 3: Illustration of the symplectic property of an integration scheme. Deviation of the numerical energy from the theorical energy ($\Delta Energy = E_{th} \quad E_{num}$) for a constant time step $\delta t = 0.1$ with $w = 0.5$ - (a) explicit Euler scheme, (b) Runge-Kutta 2 scheme, (c) Runge-Kutta 4 scheme, (d) velocity Verlet scheme.

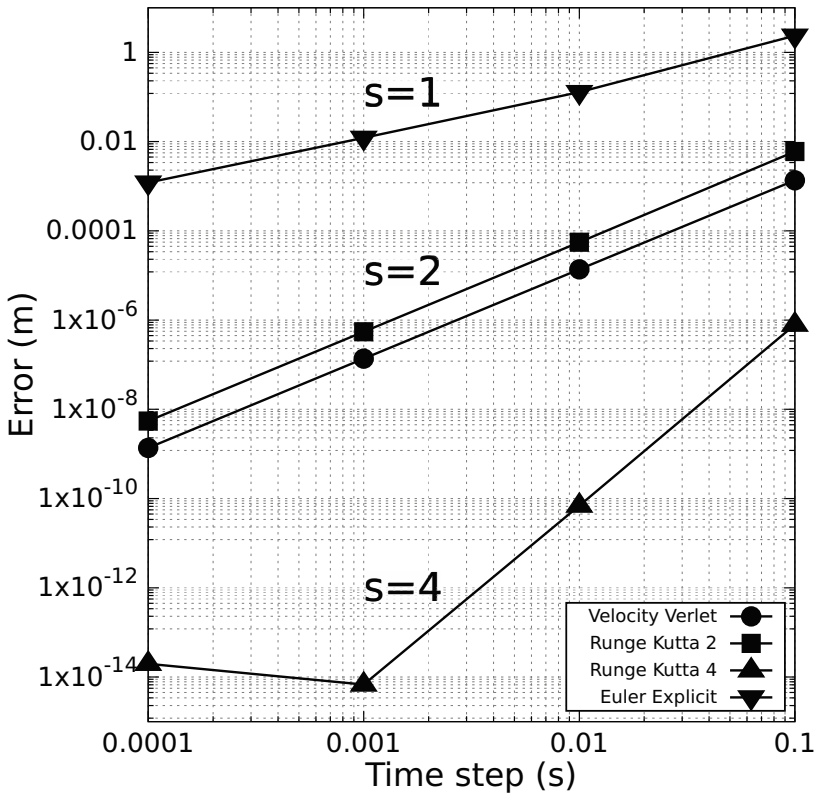

Figure 4: Illustration of the global order of convergence of different integration schemes for the harmonic oscillator: order 4 for RK4, order 2 for RK2 and velocity Verlet, and order 1 for explicit Euler, which is highlighted by the slope "**s**". We can see that for the RK4 scheme we have reached machine precision for $\Delta t = 0.001$.

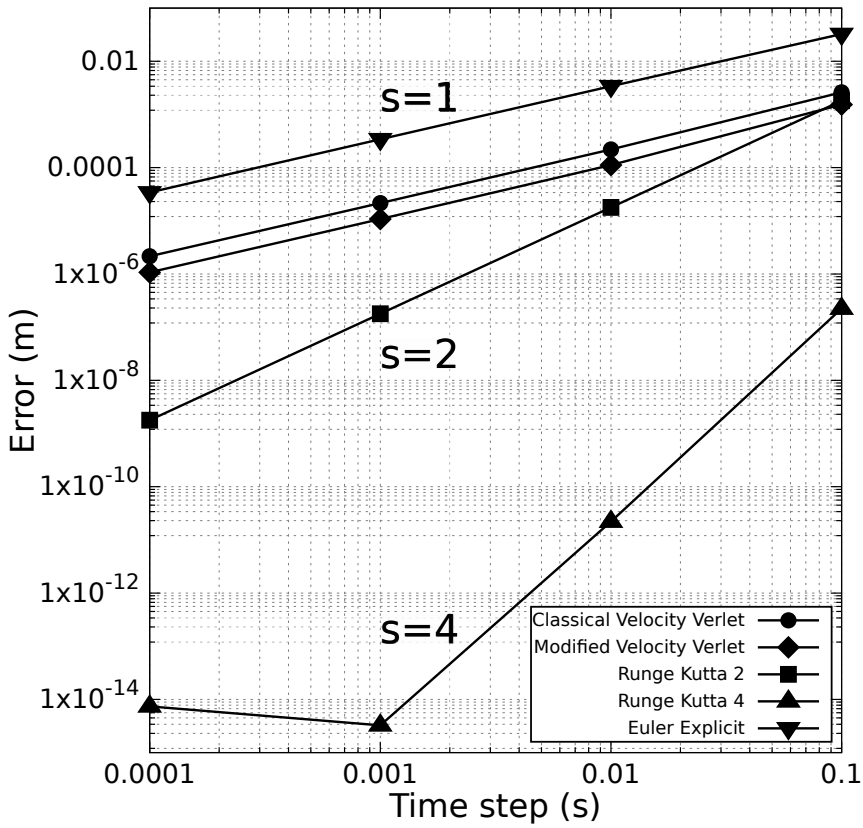

Figure 5: Illustration of the global order of convergence of different integration schemes for the damped oscillator: order 4 for RK4, order 2 for RK2, order 1 for explicit Euler and unlike the theory, order 1 for velocity Verlet, which are highlighted by the slope "**s**".

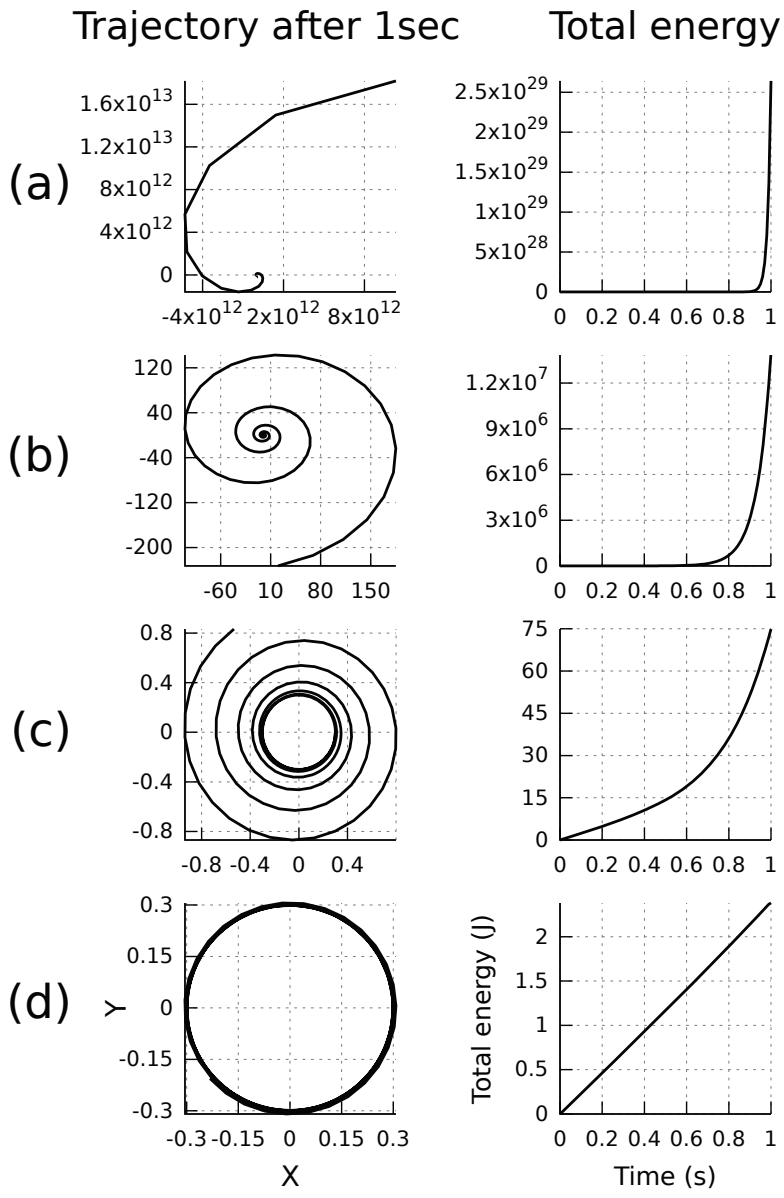

Figure 6: Representation of the trajectory after one second and of the total energy evolution in time of a particle in a rotating frame of reference ($w = 40rad/s$, $m = 1$) without any forces except Coriolis and centrifugal forces. The explicit velocity Verlet integration scheme (scheme (73)) was used with different time steps: (a) $\Delta t = 1\ 10^{-2}$, (b) $\Delta t = 1\ 10^{-3}$, (c) $\Delta t = 1\ 10^{-4}$, (d) $\Delta t = 1\ 10^{-5}$

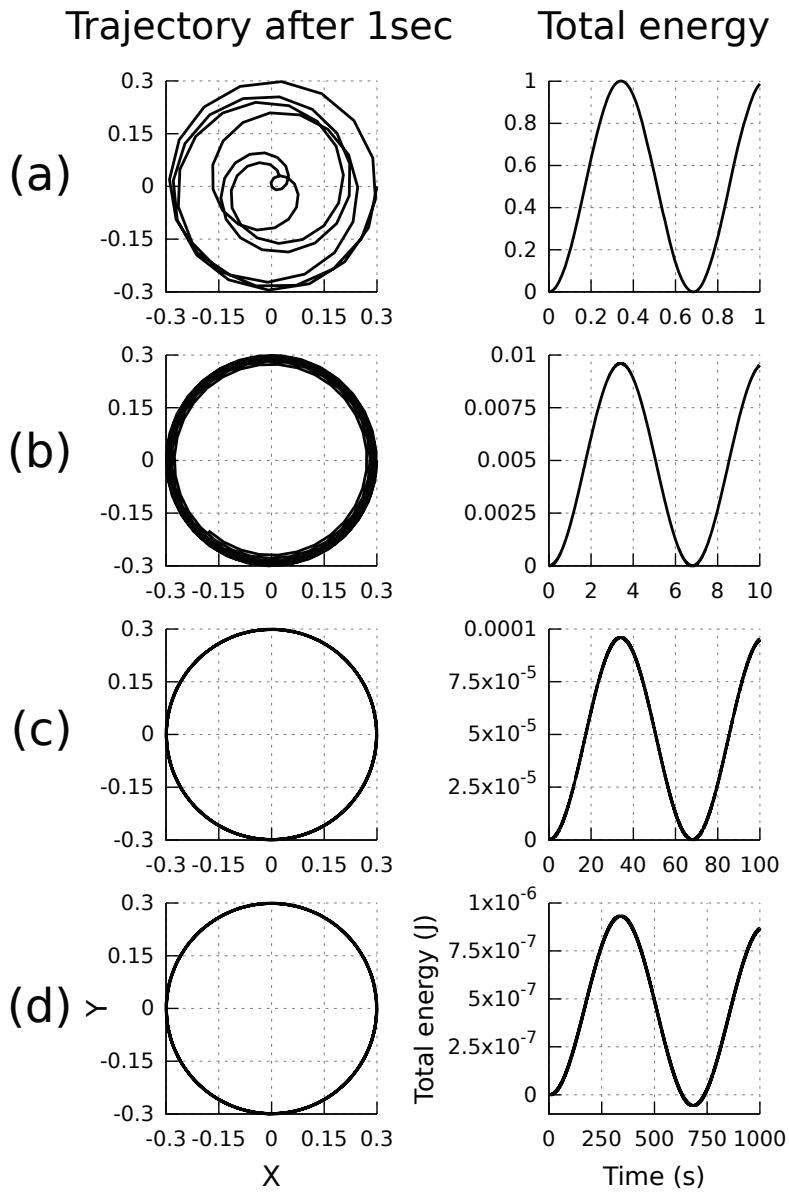

Figure 7: Representation of the trajectory after one second and of the total energy evolution in time of a particle in a rotating frame of reference ($w = 40rad/s$, $m = 1$) without any forces except Coriolis and centrifugal forces. The Scovel integration scheme was used with different time steps: (a) $\Delta t = 1 \ \ 10^{-2}$, (b) $\Delta t = 1 \ \ 10^{-3}$, (c) $\Delta t = 1 \ \ 10^{-4}$, (d) $\Delta t = 1 \ \ 10^{-5}$

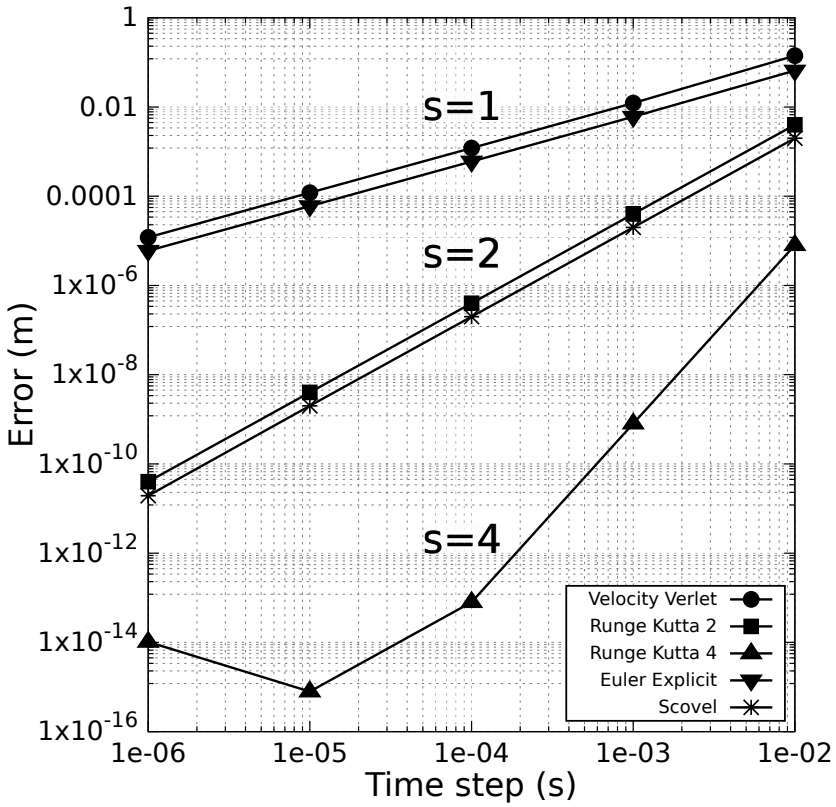

Figure 8: Illustration of the global order of convergence of different integration schemes for a particle in a non-inertial rotating frame of reference: order 4 for RK4, order 2 for RK2 and Scovel, order 1 for explicit Euler, and order 1 for velocity Verlet which are indicated by the slope "**s**".

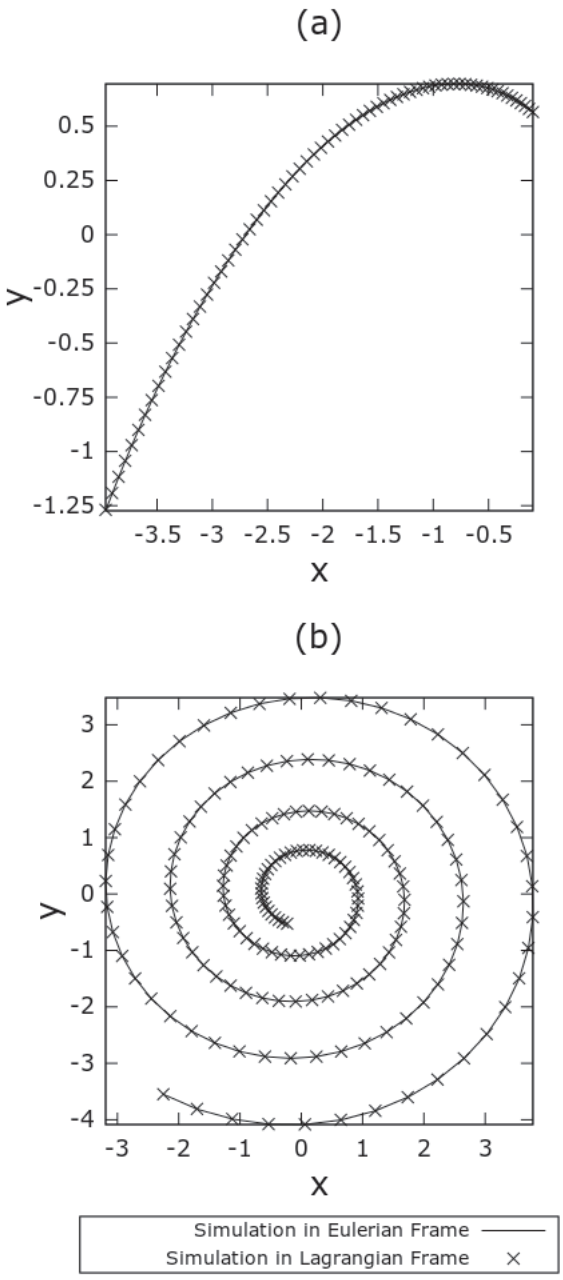

Figure 9: Trajectory of the particle in the two different frames of reference for a frame velocity of $20 rad/s$: (a) in the Eulerian frame and (b) in the Lagrangian frame

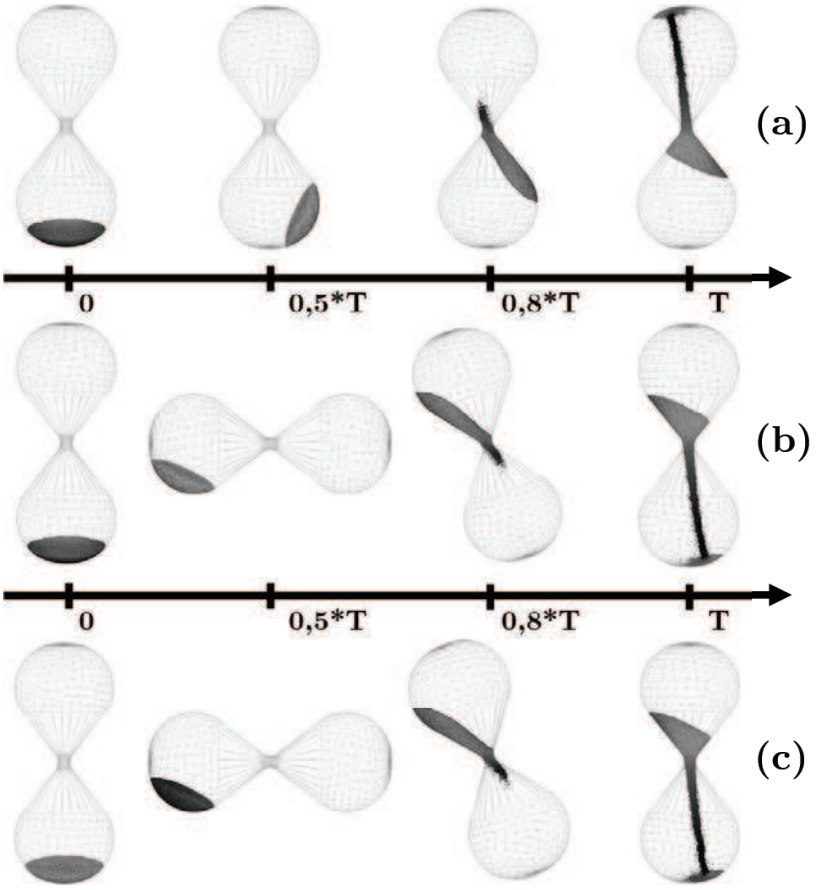

Figure 10: Motion of the particles during the revolution, of period $2T$, of an hourglass (30 RPM) - (a) Simulated in the Lagrangian frame and illustrated in the Lagrangian frame (b) Simulated in the Lagrangian frame and illustrated in the Eulerian frame (c) Simulated in the Eulerian frame and illustrated in the Eulerian frame

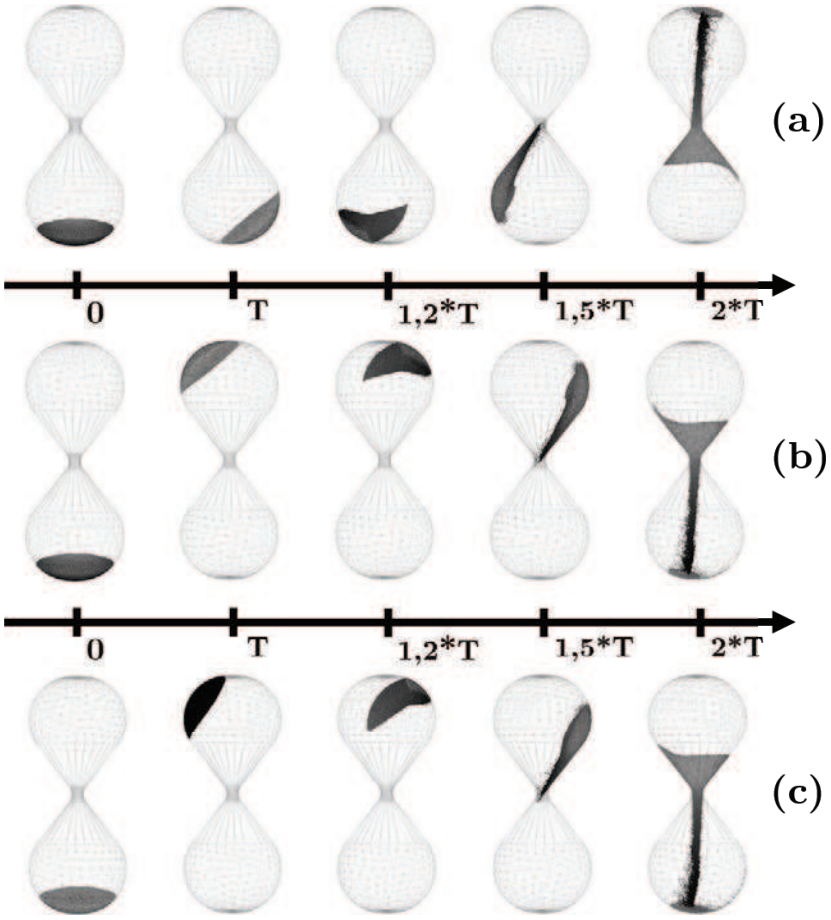

Figure 11: Motion of the particles during the revolution, of period $2T$, of an hourglass (120 RPM). From $t = T$ the rotation is stopped.- (a) Simulated in the Lagrangian frame and illustrated in the Lagrangian frame (b) Simulated inthe Lagrangian frame and illustrated in the Eulerian frame (c) Simulated in the Eulerian frame and illustrated in the Eulerian frame

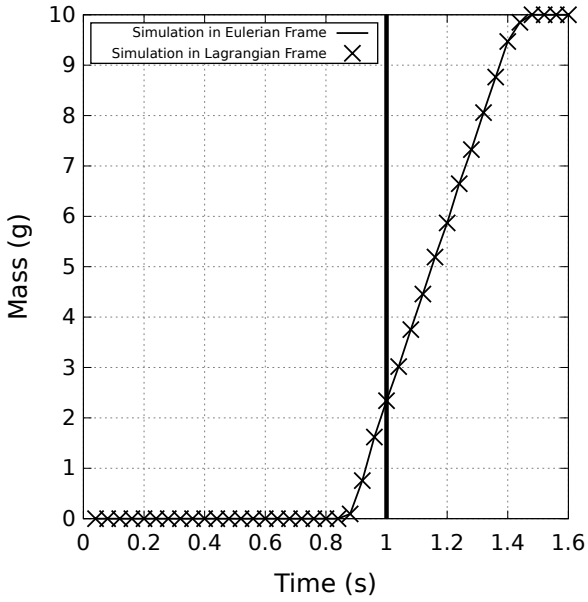

Figure 12: Comparison of the mass of particles at the bottom of the hourglass in the two different frames of reference at a frame velocity of 30 rpm ($R_o = 0.5$). The vertical bar shows the end of the rotation phase (t=T).

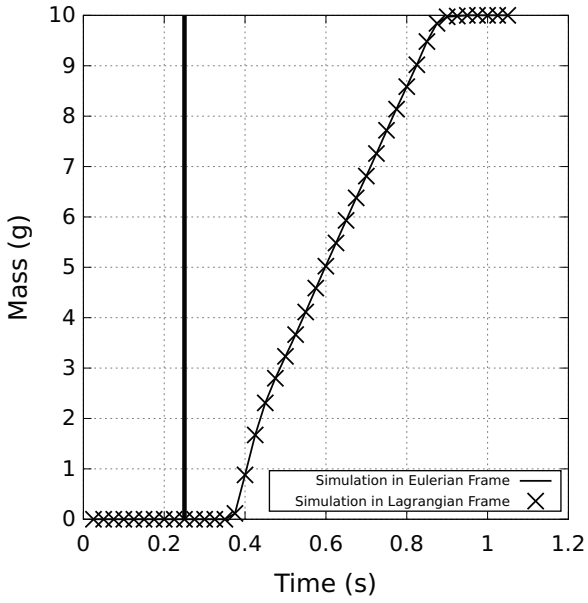

Figure 13: Comparison of the mass of particles at the bottom of the hourglass in the two different frames of reference at a frame velocity of 120 rpm ($R_o = 0$). The vertical bar shows the end of the rotation phase (t=T).

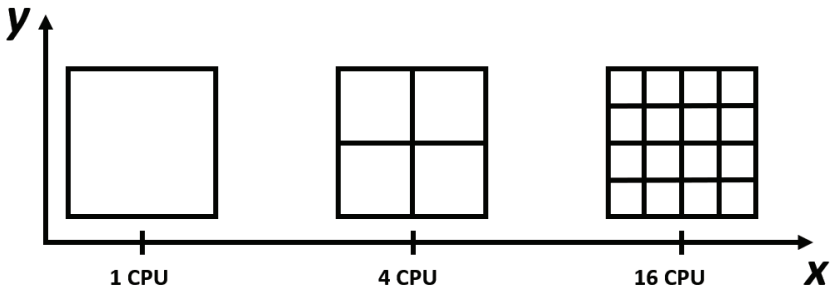

Figure 14: Distribution of the CPU in the x-y direction. Only one CPU was used in the z direction.

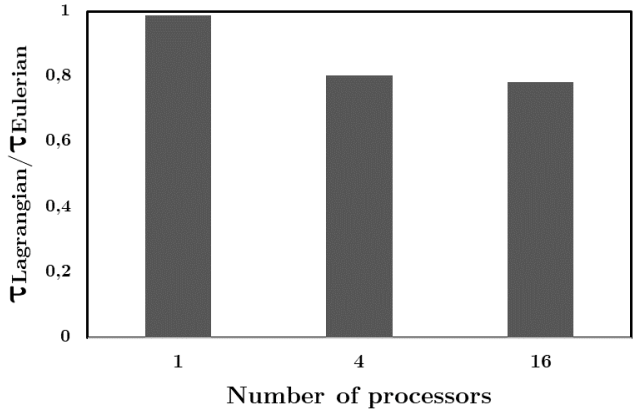

Figure 15: Ratio of the simulation time in the Lagrangian rotating frame of reference to the simulation time in the Eulerian frame of reference as a function of the number of processors for the hourglass system with 160,000 particles.

13. Tables

Parameter	Equation
Normal stiffness	$k_{n,ij} = \frac{4}{3} Y^*_{ij} \sqrt{R^*_{ij} \delta_{n,ij}}$
Tangential stiffness	$k_{t,ij} = 8 G^*_{ij} \sqrt{R^*_{ij} \delta_{n,ij}}$
Normal damping	$\gamma_{n,ij} = \quad 2\sqrt{\frac{5}{6}} \nabla \frac{\ln(e_r)}{\sqrt{\ln^2(e_r)+\pi^2}} \sqrt{\frac{2}{3} k_n m^*_{ij}}$
Tangential damping	$\gamma_{t,ij} = \quad 2\sqrt{\frac{5}{6}} \nabla \frac{\ln(e_r)}{\sqrt{\ln^2(e_r)+\pi^2}} \sqrt{k_t m^*_{ij}}$
Coulomb friction force	$\boldsymbol{f}_{ct,ij} \rightarrow \quad \mu_{s,ij} \sqrt{\boldsymbol{f}_{cn,ij}} \frac{\boldsymbol{\delta}_{t,ij}}{\sqrt{\lvert \boldsymbol{\delta}_{t,ij} \rvert}}$
Torque by tangential force	$\boldsymbol{M}_{t,ij} = \boldsymbol{r}_i \pm (\boldsymbol{f}_{ct,ij})$
Rolling friction torque	$\boldsymbol{M}_{r,ij} = \quad \mu_{r,ij} \sqrt{\boldsymbol{f}_{cn,ij}} \frac{\boldsymbol{\omega}_{p,ij}}{\sqrt{\lvert \boldsymbol{\omega}_{p,ij} \rvert}} R^*_{ij}$
Equivalent mass	$\frac{1}{m^*_{ij}} = \frac{1}{m_i} + \frac{1}{m_j}$
Equivalent radius	$\frac{1}{R^*_{ij}} = \frac{1}{R_i} + \frac{1}{R_j}$
Equivalent Young's modulus	$\frac{1}{Y^*_{ij}} = \frac{\left(1-\nu_i^2\right)}{Y_i} + \frac{\left(1-\nu_j^2\right)}{Y_j}$
Equivalent shear modulus	$\frac{1}{G^*_{ij}} = \frac{2(2+\nu_i)(1-\nu_i)}{Y_i} + \frac{2(2+\nu_j)(1-\nu_j)}{Y_j}$
Sliding friction coefficient	$\mu_{s,ij}$
Rolling friction coefficient	$\mu_{r,ij}$
Distance to contact point for particle i	$\boldsymbol{r}_i$
Radius of particle i	R_i

Table 1: Equations for the DEM model adapted from [3]

Property	**Symbol**	**Value**
Young's modulus	Y	50 MPa
Coefficient of restitution	e_r	0.3
Poisson's ratio	ν	0.3
Coefficient of friction	μ_s	0.52
Rolling friction	μ_r	0.3
DEM time step	Δt_{DEM}	$1 \pm 10^{-6} s$
Range of diameters	d_p	0.3-0.6mm
Density	ρ_p	2653 kg/m^3
Number of particle	N	160 000

Table 2: Parameters for the hourglass simulation based on a previous study that investigated the behaviour of fine particles [33]